Journal of Alloys and Compounds 1043 (2025) 184240

Contents lists available at ScienceDirect

Journal of Alloys and Compounds

journal homepage: www.elsevier.com/locate/jalcom

Comparative study of cobalt ferrite nanoparticles synthesized by solar and conventional methods

Utkirjon Sharopov [a,b,1,*], Akbarjon To'rayev [b], Siddik Kakhkhorov [b], Khusniddin Juraev [b], Otabek Kakhkhorov [b], Mirzo Sharipov [b], Muzaffar Kurbanov [c], Dilmurod Saidov [d], Odiljon Abdurakhmonov [e], Kulwinder Kaur [f], Shakeel Ahmad Khandy [g]

[a] Physical-Technical Institute, Uzbekistan Academy of Sciences, Tashkent, Uzbekistan
[b] Bukhara State University, Bukhara, Uzbekistan
[c] Urgench State University, Urgench, Uzbekistan
[d] Urgench Ranch University of Technology, Urgench, Uzbekistan
[e] Tashkent Institute of Chemical Technology, Tashkent, Uzbekistan
[f] Mehr Chand Mahajan DAV College for Women, Chandigarh, India
[g] Frontier Research Institute for Interdisciplinary Sciences, Islamic University of Science and Technology, Awantipora, India

ARTICLE INFO

Keywords:
Spinel cobalt ferrite
Solar-thermal synthesis
Large solar furnace
Crystal structure
Microchemical homogeneity
Phase composition
Electrical resistivity

ABSTRACT

This study reports the synthesis and characterization of cobalt ferrite ($CoFe_2O_4$) nanoparticles obtained via a high-temperature solar-thermal method using the Big Solar Furnace in Uzbekistan. Four different stoichiometric compositions of CoO and Fe_2O_3 were investigated to evaluate the effect of precursor ratios on phase formation, crystal structure, morphology, and electrical properties. XRF and EDX analyses confirmed the compositional variations, with the $CoFe_2O_4$ (1:2.13) sample showing the highest phase purity and minimal impurities. XRD with Rietveld refinement revealed a well-ordered cubic spinel structure, while TEM and HR-TEM analyses demonstrated nanosized crystalline particles with distinct lattice fringes. The most stoichiometric sample exhibited a maximum resistivity of 7.8×10^7 Ω·cm, which correlates with its structural ordering. DFT calculations supported the experimental findings, indicating spin-polarized band gaps and strong p–d hybridization. The obtained results were also compared with literature data for $CoFe_2O_4$ synthesized by conventional techniques (co-precipitation, sol–gel, hydrothermal), highlighting that the solar route achieves structural quality and resistivity values within the upper range of traditional methods, while offering additional benefits of eco-efficiency and scalability. This work emphasizes the potential of solar-assisted synthesis as a sustainable pathway for producing high-performance magnetic and spintronic materials.

1. Introduction

Cobalt ferrite ($CoFe_2O_4$), an anomaly among other spinel ferrites, consistently attracts the attention of various researchers across different disciplines due to its unique features and characteristics [1]. Unlike its spinel ferrite counterparts, cobalt ferrite exhibits high coercivity, excellent dielectric properties, and significant catalytic behavior, which makes it a subject of intensive study and research [2]. These materials are widely used as magnetic carriers [3], catalysts [4], sensors [5], as well as in spintronic devices [6].

One of the key factors determining the properties of $CoFe_2O_4$ spinels is their stoichiometric composition, which affects the phase composition, morphology, crystal structure, and electron density. Controlling the stoichiometry allows regulation of the phase ratio of $CoFe_2O_4$, Fe_2O_3, and CoO, which opens up new possibilities for targeted design of materials with enhanced properties. To date, many studies have been devoted to the synthesis and characterization of ferrites. The choice of synthesis method is a key factor determining the possibility of precise control over the structure and properties of ferrites, which is critically important for meeting the demands of modern magnetoelectronic technologies [7]. Current research in the field of magnetic ferrite synthesis demonstrates a wide range of methodological approaches aimed

* Correspondence to: Solar thermal and power plants" laboratory, Physical-Technical Institute, Chingiz Aitmatov St., 2, Tashkent 100084, Uzbekistan.
E-mail address: utkirstar@gmail.com (U. Sharopov).
[1] https://orcid.org/0000-0002-7962-0426

https://doi.org/10.1016/j.jallcom.2025.184240
Received 15 August 2025; Received in revised form 26 September 2025; Accepted 5 October 2025
Available online 8 October 2025

at optimizing the structural and functional properties of nanostructured materials for innovative technological applications [8]. Despite significant progress in the development of chemical synthesis methods, including thermal decomposition of precursors, solvothermal processes, co-precipitation, and auto-combustion, systematic analysis of the correlation between synthesis conditions, particle morphology, and their magnetic characteristics remains a relevant task [9,10]. Here in the introduction, we briefly present the main methods for obtaining ferrites and their characteristic features.

1. The hydrothermal method for obtaining ferrites is based on the reaction of precursors in an aqueous medium at elevated temperature and pressure. This process allows the production of highly crystalline nanoparticles (10–100 nm) with minimal defects, such as Gd-doped cobalt ferrites [11,12]. The absence of the need for high-temperature calcination prevents grain growth; however, the risk of forming intermediate phases (Fe_2O_3, $BaCO_3$) and the high energy consumption limit its industrial application [13,14].
2. The sol-gel technology, in turn, ensures chemical homogeneity through the step-by-step formation of a sol and gel from metal salt solutions. The low synthesis temperatures (~400°C) preserve the nanostructure, as demonstrated in the case of M-type barium ferrite ($BaFe_{12}O_{19}$) with a resistance of 10^2–10^4 Ohm. However, the long duration of the process, high cost of precursors, and low productivity make the method more suitable for laboratory research than for mass production [15,16].

3. The co-precipitation method stands out for its simplicity and cost-effectiveness. The precipitation of metal ions from solution followed by calcination allows for the rapid production of materials such as $NiFe_2O_4$ [17]. However, incomplete precipitation and uneven distribution of dopant elements lead to low crystallinity and resistance in the range of 10^4–10^6 Ohm, which limits their application in high-precision devices [18].
4. Microemulsion synthesis, using a "water-oil-surfactant" system, provides precise control over particle morphology. For example, Fe_3O_4/Ag composites synthesized by this method exhibit high dispersity and low resistance (10^3–10^5 Ohm) [19,20]. Nevertheless, the need for expensive surfactants and the complexity of removing organic residues hinder scalability [21].
5. Solid-state sintering, traditionally used in industry, is based on mechanical mixing of oxides followed by sintering at temperatures above 1200°C. Despite its simplicity and suitability for mass production, the method leads to the formation of large grains (1–10 μm) and high porosity, which increases resistance up to 10^6–10^8 Ohm [22]. Modern modifications, such as spark plasma sintering (SPS), partially solve these problems but remain energy-intensive [23]. Table 1 contains the main methods for synthesizing ferrite materials.

In recent years, “green” routes to ferrites have advanced rapidly, including biogenic syntheses (using plant extracts), hydro/solvothermal and microwave regimes, mechanochemistry, and low-temperature schemes employing molten salts and deep eutectic solvents (DES) [27,28]. These approaches reduce the thermal budget and processing time, improve dispersion and the crystal chemistry of spinels, and minimize toxic reagents; however, most still rely on electric heating (often energy-intensive at scale) and require narrowly tuned chemistries to stabilize phase and texture [29,30]. Contemporary reviews from 2023 to 2025 systematize these strategies for spinel ferrites ($CoFe_2O4$, $MnFe_2O_4$, $ZnFe_2O_4$, etc.), highlighting the advantages of microwave acceleration (minute-scale syntheses and a smaller carbon footprint), controlled hydro/solvothermal processing, biogenic reductive–chelating media, and mechanochemistry as a low-temperature route that nevertheless often requires post-annealing to achieve lattice ordering [31–34].

Against this backdrop, the use of concentrated solar energy in a Large Solar Furnace (LSF) provides a distinct thermotechnological pathway for green synthesis: replacing electricity with direct solar heat delivered at high flux densities and temperatures up to 1500–2000 °C, thereby accelerating solid-state transformations, shortening dwell times, and lowering the carbon footprint of thermal treatment [35,36]. Recent reviews on materials processed in solar furnaces document growing interest in solar-thermal processing and the synthesis of oxides/ceramics, and they demonstrate the industrial potential of megawatt-class facilities (for example, the Parkent LSF in Uzbekistan with power up to ~1 MW and concentration ratios of ~4500–10,000) [37]. Publications specifically on ferrites synthesized in solar furnaces remain scarce: examples exist for nickel ferrite, whereas systematic studies on cobalt ferrite are, to our knowledge, rare. This underscores the relevance and novelty of our approach.

In this context, we propose using the LSF as a green source of high-temperature heat for the heat-treatment stage of $CoFe_2O_4$, as an alternative to electric muffle/tube furnaces and as a complement to solution chemistry. The key contributions of this work are threefold: we employ the LSF to obtain the spinel with a targeted cation distribution and high crystallinity under a reduced thermal budget; we demonstrate magnetic properties comparable to or better than those achieved by electric heating while shortening the dwell time; and we discuss the scalability of the approach on megawatt-class installations and its integration with low-temperature stages (precipitation/gel), without increasing the chemical “toxicity” of the process. Compared with alternatives (microwave and hydrothermal treatments, mechanochemistry), our route removes the electrical component from the high-temperature stage and harnesses renewable heat delivered at high radiative flux.

As can be seen, the choice of synthesis method is determined by the requirements for crystallinity, electrical properties, and scalability. Combined approaches, such as in-situ formation of composites, open new opportunities for optimizing ferrite characteristics [38]. Based on the above, a high-temperature Big Solar Furnace was used for the synthesis of cobalt ferrite to ensure a high level of purity and uniformity of the synthesis process. The obtained results were compared with data obtained using other methods. In addition, we varied the stoichiometric composition of the precursors, which has a significant impact on the phase composition, morphology, crystal structure, and electron density of the resulting material. Precise control of stoichiometry allows regulation of the phase ratio of $CoFe_2O_4$, Fe_2O_3, and CoO, opening up new possibilities for targeted design of materials with improved functional characteristics.

In this work, a comprehensive study of $CoFe_2O_4$ spinels with various stoichiometric compositions was carried out, including analysis of their

Table 1
Summarizes the main methods for synthesizing ferrite materials.

Synthesis Method	Crystallinity	Sample Resistivity	Comments
Hydrothermal [12,13]	High	Low (10^3–10^5 Ω)	Homogeneous nanoparticles with minimal defects. Intermediate phases may increase resistivity.
Sol-gel [16,17,24]	Medium–High	Low (10^2–10^4 Ω)	High purity, but heat treatment may affect density.
Co-precipitation [18,25]	Low–Medium	Medium–High (10^4–10^6 Ω)	Incomplete precipitation and impurities increase resistivity.
Microemulsion [19,20]	High	Low (10^3–10^5 Ω)	Particle size control reduces defectiveness, but scalability is limited.
Solid-state sintering [22,23,26]	High	High (10^6–10^8 Ω)	Large grains and pores create charge transport barriers.

electron density, morphology, and crystal structure. X-ray fluorescence analysis (XRF), X-ray diffractometry (XRD), as well as high-resolution transmission electron microscopy (HR-TEM) and energy-dispersive spectroscopy (EDX) made it possible to obtain a detailed understanding of the relationship between composition and structural characteristics of these materials. The main objective of this study is to determine the effect of stoichiometric composition on the phase composition, crystal structure, and electronic properties of $CoFe_2O_4$ spinels, which opens up prospects for their application in high-tech devices and allows optimization of the synthesis process to achieve the desired properties. The obtained data will also contribute to further studies aimed at investigating the electronic structure using methods of electron spectroscopy and microscopy [39].

2. Synthesis method of cobalt ferrite materials

In this work, the Big Solar Furnace located in the Parkent district of the Republic of Uzbekistan was used for the synthesis of cobalt ferrite ($CoFe_2O_4$) structures. The samples were prepared from mixtures of cobalt oxide (CoO) and iron oxide (Fe_2O_3) in stoichiometric ratios (Table 2). The proposed synthesis scheme is illustrated in Fig. 1.

Then these samples were placed on a water-cooled melting unit located in the focal plane of the solar furnace [40,41]. A concentrated solar radiation flux with a power density of approximately Q $= 150$ W/cm^2 was directed onto the sample. At this temperature, the sample begins to melt. After that, droplets of the melt fall into water and are cooled at a rate of 10^3 °C/s. Such cooling conditions allow for the preservation of the high-temperature structural states of the material [42]. The melt droplets fractured into small glassy particles of arbitrary shape upon immersion in water. The melted material was then ground in a laboratory ball mill. After grinding and semi-dry pressing (at 100 MPa), cylindrical samples with a diameter of 10 mm were obtained. The pressed and powdered samples were sent for further investigation.

Ball milling was used solely for mechanical size reduction of the already synthesized material and did not induce any chemical changes or phase transformations, as confirmed by the consistency of XRD patterns before and after the milling process.

2.1. Large solar furnace (LSF), parkent (Uzbekistan)

Experiments were conducted at the megawatt-class Large Solar Furnace (LSF) in Parkent (Uzbekistan). The facility comprises a field of heliostats that redirect sunlight onto a segmented parabolic concentrator; a high heat-flux zone is formed at the focal test plane (Fig. 2). According to the literature for the Parkent LSF, the maximum usable thermal power is on the order of 0.7–1.0 MW, the concentration ratio is ~4500–10,000, and the focal temperature exceeds 1500–2000 °C (and can be higher with suitable absorbers). The characteristic size of the working light spot can be adjusted by defocusing and varies from a few to several tens of centimeters. These parameters and operating regimes are described in detail in review and technical sources on the Parkent LSF [41,42].

Heating rates and the temperature profile were controlled by a combination of defocus and shutter position. To ensure comparability of thermal budgets between runs, we recorded direct normal irradiance (DNI), the shutter position/degree of defocus, and the time-resolved temperature T(t) at a sampling rate of 1–10 Hz.

Table 2
Ratios of cobalt and iron oxide mixtures (CoO + Fe_2O_3).

Sample No.	CoO:Fe_2O_3 Ratio	CoO Mass (g)	Fe_2O_3 Mass (g)	Total Mixture Mass (g)
No.1-$Co_3FeO_{1.2}$	3:1	24	8	32
No.2-$CoFeO_{2.5}$	1:1	15	15	30
No.3-$CoFe_2O_4$	1:2.13	10	21	31
No.4-$CoFe_{2.8}O_4$	1:3	8	24	32

3. Methods for analyzing material characteristics

3.1. X-ray diffraction (XRD) and rietveld refinement

To investigate the crystal and electronic structure of CoFe2O4 synthesized by the solar method, modern diffractometric and modeling analysis techniques were applied. The primary tool was XRD, and the data were interpreted using the Rietveld method with the FullProf Suite software package. This allowed refinement of the crystal lattice parameters, symmetry, space groups, and atomic coordinates in the unit cell.

3.2. Crystal structure visualization using VESTA

To visualize the crystal structure and analyze the distribution of atoms in the volume, the VESTA program was used. It enabled the construction of three-dimensional models of the unit cells of $CoFe_2O_4$, CoO, and Fe_2O_3 phases [44], determination of the type of coordination of ionic positions, bond lengths, and angles between coordination polyhedra. These data formed the basis for spatial mapping of phase inclusions and domain structure.

3.3. Electron density mapping (GFourier Method)

Additionally, the electron density mapping method implemented in the GFourier program was applied. The electron density was calculated based on the Fourier transform of structural factors obtained from XRD. Both three-dimensional (3D) and two-dimensional (2D) electron density maps were constructed, which allowed visualization of the distribution of electrons between atoms and within coordination nodes. The analysis of electron density revealed key regions of interatomic interactions, the nature of charge distribution, and the presence of a covalent component in the bonds, significantly complementing the structural information obtained from X-ray diffraction.

3.4. Transmission and scanning electron microscopy (TEM, HR-TEM, STEM-EDX)

Powders were ultrasonically dispersed (5–10 min) in ethanol and drop-cast onto holey-carbon Cu grids, then air-dried. Conventional TEM surveys were acquired on a JEOL JEM-1011 (BF, 100 kV) and on a Thermo Fisher Talos 200i in TEM mode (200 kV). HR-TEM lattice imaging, STEM, and EDX mapping were performed on the Talos 200i (HT 200 kV; typical STEM mapping: 64.4 kx, 1.55 μm field, 3.031 nm pixel, 20 μs dwell). SAED and FFTs were used to index reflections and measure d-spacings of the spinel phase. Particle-size statistics ($n \geq 200$) were extracted from low-mag TEM images in ImageJ (thresholding with manual correction). Carbon signals in EDX maps were treated as support-film background.

3.5. X-ray powder diffraction and phase identification

The phase analysis of the samples was conducted using X-ray diffraction on polycrystalline powders. The diffraction patterns were collected using a D2 Phaser instrument model Bruker-AXS (Germany) with CuKα radiation and a graphite monochromator ($\lambda = 1.54178$ Å). The instrument was operated in tube mode (Cu) with a current of 10 mA and a voltage of 30 kV. The angle 2θ range was from 10° to 75° with a step of 0.02°. The slit was adjusted to 0.6 mm, and the exposure time at a given point was 1 s, with the energy discriminator ranging from 0.17 to 0.23 keV. Spectrum analysis and phase identification were performed

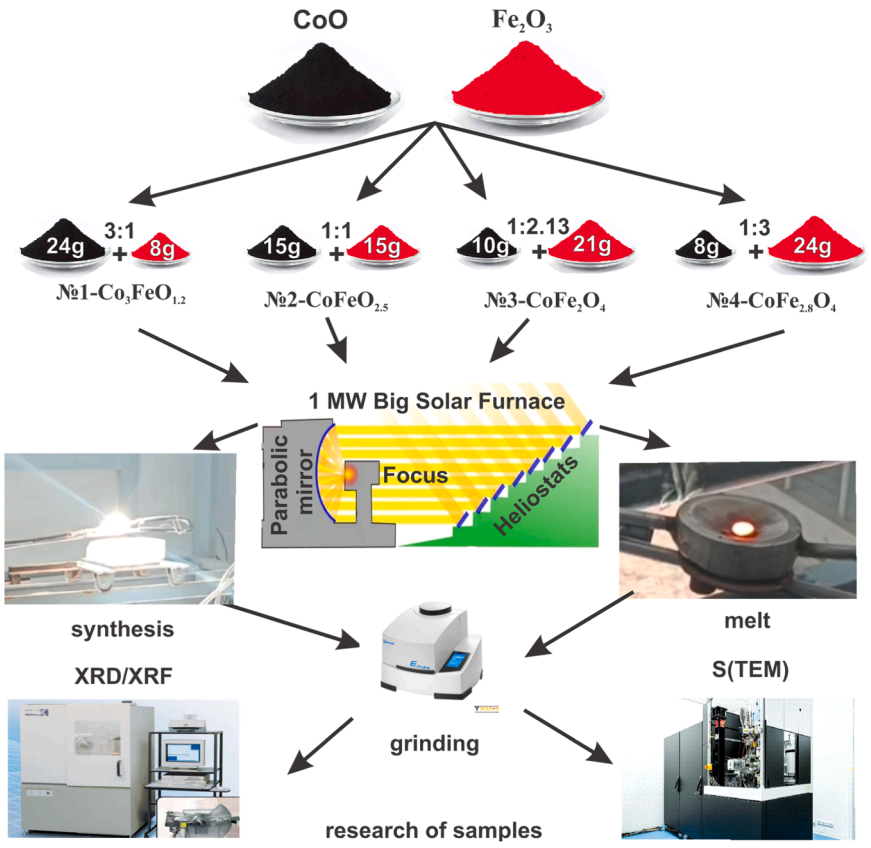

Fig. 1. Scheme for obtaining cobalt ferrite nanoparticles.

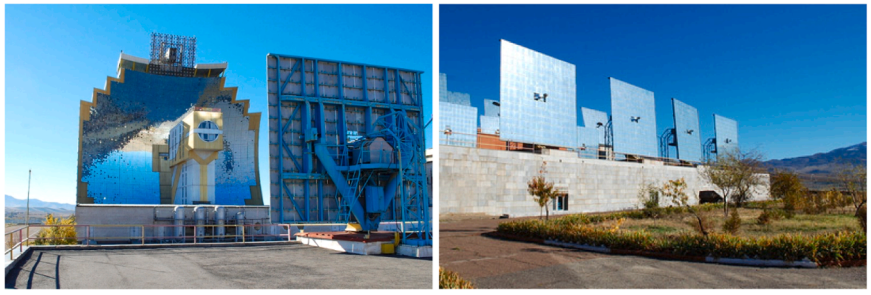

Fig. 2. Large Solar Furnace (LSF), Parkent, Uzbekistan: (a) segmented parabolic concentrator and focal tower; (b) heliostats field [43].

using the JCPDS-ICDD library and specialized software.

3.6. Electrical resistivity measurements (Van der Pauw Method)

To evaluate the electrical properties of the synthesized $CoFe_2O_4$ spinels with varying stoichiometries, resistivity (ρ) measurements were performed using the four-point probe Van der Pauw method (ST2258C instrument).

3.7. Density functional theory (DFT) calculations

For theoretical comparison, first-principles density functional theory (DFT) calculations were carried out using Quantum ESPRESSO. The electronic structure and charge distribution were analyzed to correlate the experimental resistivity data with the predicted electronic properties. A detailed description of these methods and the results obtained for other samples can be found in [45–48]. We make use of PBE-GGA and PBE-GGA+*U* to optimize the electronic structures of CoO and $CoFe_2O_4$ and the detailed discussion cab be seen in Section 4.7. A detailed description of these methods and the results obtained for other samples can be found in [49,50].

3.8. Dynamic light scattering (DLS)

The hydrodynamic particle size distribution was determined using dynamic light scattering (DLS) on a JL-1197 analyzer (Chengdu Jingxin Powder Testing Equipment Co., Ltd., China). The powder was dispersed in water at a low concentration; the suspension was sonicated for 5 min and measured in quartz cuvettes at 25 ± 0.5 °C. Three independent measurements were performed for each sample; the results are presented as mean ± SD.

4. Results and discussion

4.1. XRF analysis of the obtained cobalt ferrite spinels

At the first stage of the work, we conducted a study of cobalt ferrite spinel samples with different stoichiometric compositions synthesized

using a solar furnace. Data on the oxide composition of the samples based on XRF results are presented in Table 3.

During the study of sample No. 1 synthesized using the solar furnace, XRF analysis made it possible to determine its chemical oxide composition. According to the analysis results (Table 3), the main components are cobalt oxide (CoO) – 64.8 wt% and iron oxide (Fe_2O_3) – 26.4 wt%. The sample also contained impurities, including manganese oxide (MnO) – 0.764 wt%, aluminum oxide (Al_2O_3) – 0.228 wt%, silicon oxide (SiO_2) – 0.233 wt%, and zirconium oxide (ZrO_2) – 0.197 wt%. Additionally, small amounts of sulfur oxide (SO_3) – 0.0259 wt%, chromium oxide (Cr_2O_3) – 0.0495 wt%, and tin oxide (SnO_2) – 0.0102 wt% were recorded.

XRF analysis of sample No. 2 showed the formation of a compound with a deviation from the ideal stoichiometric composition, containing cobalt oxide (CoO) – 48.0 wt% and iron oxide (Fe_2O_3) – 50.3 wt% (Table 3). Impurities include MnO (0.531 wt%), Al_2O_3 (0.226 wt%), ZrO_2 (0.237 wt%), and SiO_2 (0.225 wt%).

In sample No. 3, the phase composition is closest to the theoretical one. The main elements include cobalt oxide (CoO) – 31.5 wt% and iron oxide (Fe_2O_3) – 67.1 wt% (Table 3). The impurity content is minimal: MnO (0.337 wt%), Al_2O_3 (0.197 wt%), ZrO_2 (0.328 wt%), and SiO_2 (0.197 wt%).

Sample No. 4 is characterized by an increased iron (Fe) content – 73.7 wt% and a reduced cobalt (Co) content – 24.8 wt% (Table 3). Impurities include MnO (0.402 wt%), Al_2O_3 (0.202 wt%), ZrO_2 (0.255 wt %), and SiO_2 (0.182 wt%).

The XRF results showed that changes in the stoichiometric composition of cobalt ferrites directly affect their oxide composition (Table 3). In sample No. 1, a high content of CoO (64.8 wt%) and a relatively low content of Fe_2O_3 (26.4 wt%) were observed. This indicates an excess of cobalt relative to iron in the initial composition, leading to the formation of a compound with a deviation from the ideal stoichiometric composition.

With increasing iron and decreasing cobalt, the trend of decreasing CoO and increasing Fe_2O_3 is most pronounced in sample No. 3; for sample No. 2 the change is minor and within the uncertainty of the XRF oxide composition (see Table 3). In sample No. 3, a nearly ideal ratio of the main oxides is achieved: CoO accounts for 31.5 wt% and Fe_2O_3 for 67.1 wt%, which corresponds to theoretical calculations for this stoichiometry.

With a further increase in iron content, as seen in sample No. 4, the Fe_2O_3 content rises to 73.7 wt%, while the CoO content decreases to 24.8 wt%. This confirms the dependence of the oxide composition on the stoichiometric ratio of cobalt and iron in the sample.

Thus, the conducted XRF study demonstrated the relationship between the stoichiometric composition of cobalt ferrites and their oxide composition, as well as revealed the presence of impurities. Further investigation of the phase composition of the obtained samples was carried out using XRD.

Table 3
XRF analysis data of cobalt ferrites with various stoichiometric compositions.

	No.1- $Co_3FeO_{1.2}$	**No.2-** $CoFeO_{2.5}$	**No.3-** $CoFe_2O_4$	**No.4-** $CoFe_{2.8}O_4$
Comp.	Content, mass, %			
Cl	0.0080	0.0401	0.0065	0.0064
Al_2O_3	0.2280	0.2260	0.1970	0.2020
SiO_2	0.2330	0.2250	0.1970	0.1820
SO_3	0.0259	0.0409	0.0248	0.0247
Cr_2O_3	0.0495	0.0440	0.0358	0.0390
MnO	0.7640	0.531	0.3370	0.4020
Fe_2O_3	**26.4**	**50.3**	**67.1**	**73.7**
CoO	**64.8**	**48.0**	**31.5**	**24.8**
ZrO_2	0.1970	0.2370	0.3280	0.2550
SnO_2	0.0102	0.0108	0.0658	0.1270

4.2. XRD analysis of the obtained cobalt ferrites

Fig. 3 presents the X-ray diffraction patterns of $CoFe_2O_4$ samples with different stoichiometric compositions.

To identify the phases in the samples, the Match! 4 software with the PDF-2 database was used, allowing composition determination based on JCPDS data matching.

Sample (a) No. 1 (Fig. 3a, purple curve):

The main cobalt ferrite phase was identified according to JCPDS No. 96–153–3164, with prominent peaks at 2θ: 30.17°, 35.53°, 43.18°, 57.11°, 62.71°, and 74.20°, corresponding to (hkl) planes: 202, 311, 400, 511, 404, and 533. The cubic structure of this phase has unit cell parameters a = b = c = 8.3806 Å and belongs to space group Fd-3m (227).

The Fe_2O_3 phase was also present, identified by JCPDS No. 96–230–0618, with less intense peaks at 2θ: 30.32°, 35.72°, 43.42°, 57.44°, 63.09°, and 74.90°, unit cell parameters a = b = c = 8.3364 Å, and space group P4332 (212).

The CoO phase was identified by JCPDS No. 96–153–3088, with diffraction peaks at 2θ: 36.71°, 42.65°, 61.90°, 74.17°, and 78.16°, corresponding to (hkl) planes: 111, 200, 202, 311, and 222. Phase analysis revealed that the $Co_3FeO_{1.2}$ sample consists of 4.4 % $CoFe_2O_4$, 59.2 % CoO, and 36.4 % Fe_2O_3.

In sample No. 2 (Fig. 3b, black curve), three phases were also detected. The cobalt ferrite content is 39.8 %, CoO – 32.8 %, and Fe_2O_3 – 27.3 %. As the stoichiometric ratio of CoO increases and Fe_2O_3 decreases, the $CoFe_2O_4$ phase content rises.

The composition of sample No. 3 (Fig. 3c, pink curve) shows the highest concentration of the $CoFe_2O_4$ phase among the samples. Phase analysis indicated that the sample consists of 58.1 % $CoFe_2O_4$, 18.5 % CoO, and 23.4 % Fe_2O_3. This composition is the closest to the theoretical value for pure $CoFe_2O_4$.

In sample No. 4 (Fig. 3d, green curve), the $CoFe_2O_4$ phase content is reduced compared to the previous samples, amounting to 27.9 %, while CoO and Fe_2O_3 contents increased to 24.3 % and 47.8 %, respectively.

Thus, among the presented samples, the highest content of the $CoFe_2O_4$ phase is observed in the sample with the empirical formula $CoFe_2O_4$, corresponding to its theoretical composition. These results highlight the importance of precise stoichiometric control to achieve desired phase compositions and material properties.

Powder diffraction patterns were refined by the Rietveld method using the FullProf packages in a multi-phase setup with simultaneous

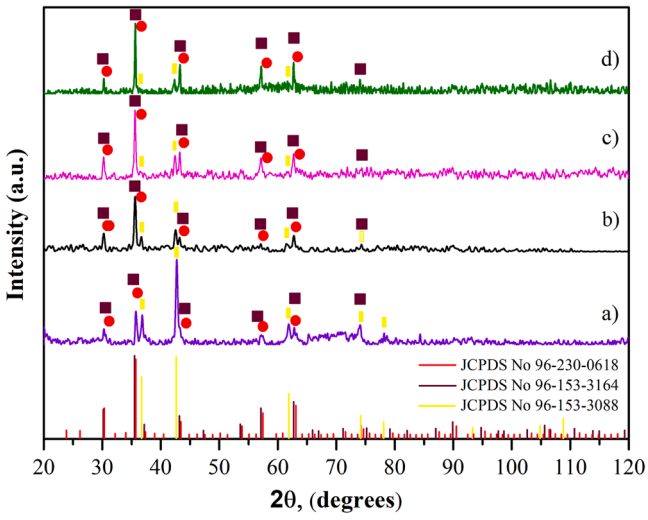

Fig. 3. X-ray diffraction patterns of cobalt ferrites with different stoichiometric compositions: a) No. 1 – $Co_3FeO_{1.2}$ (purple curve), b) No. 2 – $CoFeO_{2.5}$ (black curve), c) No. 3 – $CoFe_2O_4$ (pink curve), and d) No. 4 – $CoFe_{2.8}O_4$ (green curve).

refinement of all present phases. The structural models employed were: spinel $CoFe_2O_4$ (space group Fd-3m, cation at 8a/16d and O at 32e), hematite α-Fe_2O_3 (R-3c), and cobalt(II) oxide CoO (rock-salt, Fm-3m). All measurements used Cu Kα radiation (λ = 1.54178 Å); the working range was 2θ = 20–120° with a step of 0.02°. Peak profiles were modeled with a pseudo-Voigt function (Thompson–Cox–Hastings, TCH), and the background with a Chebyshev polynomial (order ≥ 5). Jointly for all phases we refined the scale factors (with subsequent calculation of weight fractions via the Hill–Howard method), the zero shift Δ2θ, and profile parameters (Caglioti model: U–V–W); for each phase separately we refined the lattice parameter(s) and microstructural parameters (crystallite size D and microstrain ε). When preferred orientation was evident, the March–Dollase model was applied (phase-

dependent). The instrumental contribution to peak broadening was evaluated from a standard reference scan and accounted for when extracting D and ε. Uncertainties are reported as standard errors (1σ) from the covariance matrix. Goodness of fit was assessed by Rp, Rwp, Rexp, and χ^2; comprehensive refinement outputs (including phase weight fractions and D and ε for each phase) are summarized in Table 4.

Structural metrics track phase purity as well: sample No. 3 shows a larger crystallite size (D) and lower microstrain (ε) than samples with higher CoO/Fe_2O_3 content, indicating a more ordered spinel lattice and reduced defectiveness of the $CoFe_2O_4$ matrix.

4.3. Electronic structure of the obtained cobalt ferrites

To gain deeper insight into the internal structure of the $CoFe_2O_4$ compound, the electron density mapping method was applied (Fig. 4a, b). This approach enables visualization of the electron distribution within the unit cell and identification of the precise positions of atoms constituting the crystal. The electron density is calculated using a Fourier transform applied to the geometrical structure factors, providing a detailed representation of the atomic structure in three-dimensional (3D) or two-dimensional (2D) forms. The GFourier program from the FullProf package was used to construct these maps, offering a powerful tool for analyzing electron scattering and material structures.

The 3D electron density map visualizes the distribution of electrons around the Co, Fe, and O atoms within the $CoFe_2O_4$ unit cell. The map shows regions of high electron density (depicted as orange zones), corresponding to the positions of metal atoms, and regions of low density (blue zones) located between the atoms. Fe^{3+} atoms, occupying octahedral positions, generate local density maxima, indicating strong electron attraction to their nuclei. Co^{2+} atoms in tetrahedral sites are surrounded by smaller density regions, reflecting their coordination with four O^{2-} ions.

O^{2-} ions form dense trigonal pyramids, linking metal atoms in a three-dimensional network through shared corners or edges. Their electron density is evenly distributed between Co and Fe atoms, forming stable bonds.

Data obtained using the VESTA program confirm that the $CoFe_2O_4$ structure belongs to the cubic space group Fd-3m. Fe^{3+} ions occupy octahedral positions (16d), Co^{2+} ions are located in tetrahedral positions (8a), and O^{2-} ions occupy 32e positions, forming the spatial lattice. The lattice parameter is 8.399 Å, which is consistent with experimental data.

The 2D electron density map presented in Fig. 4b shows a cross-section through the plane of the unit cell, allowing analysis of the electron density distribution in the selected area. The orange contours on the map represent regions of maximum electron density corresponding to the Co and Fe atoms. These areas illustrate how electrons are distributed around the central atoms in tetrahedral and octahedral positions. The light blue zones indicate regions of minimal electron density, corresponding to interatomic spaces. The map clearly demonstrates the bonding between metal and oxygen atoms. The elongated electron clouds along bond directions indicate a strong covalent component in the interatomic interactions.

Particular attention is drawn to regions where CoO_4 tetrahedra and

Table 4
Rietveld agreement factors and microstructural parameters (D, ε) for multi-phase XRD models.

Sample	Profile fn	Background	Zero shift (°)	Rp (%)	Rwp (%)	Rexp (%)	χ^2	Crystal size (nm)	σ (D) (nm)	ε (×10⁻⁴)	σ(ε) (×10⁻⁴)	χ^2	Provenance
No.1 ($Co_3FeO_{1.2}$)	Pseudo-Voigt	Chebyshev (order ≥5)	−0.02	8.1	10.6	6.6	2.58	24	3	65	7	2.58	FullProf output
No.2 ($CoFeO_{2.5}$)	Pseudo-Voigt	Chebyshev (order ≥5)	−0.01	8.5	11.2	6.8	2.71	28	3	55	6	2.71	FullProf output
No.3 ($CoFe_2O_4$)	Pseudo-Voigt	Chebyshev (order ≥5)	0	6.7	8.8	5.5	2.56	36	3	38	5	2.56	FullProf output
No.4 ($CoFe_{2.8}O_4$)	Pseudo-Voigt	Chebyshev (order ≥5)	0.01	7.3	9.5	5.9	2.59	32	3	45	5	2.59	FullProf output

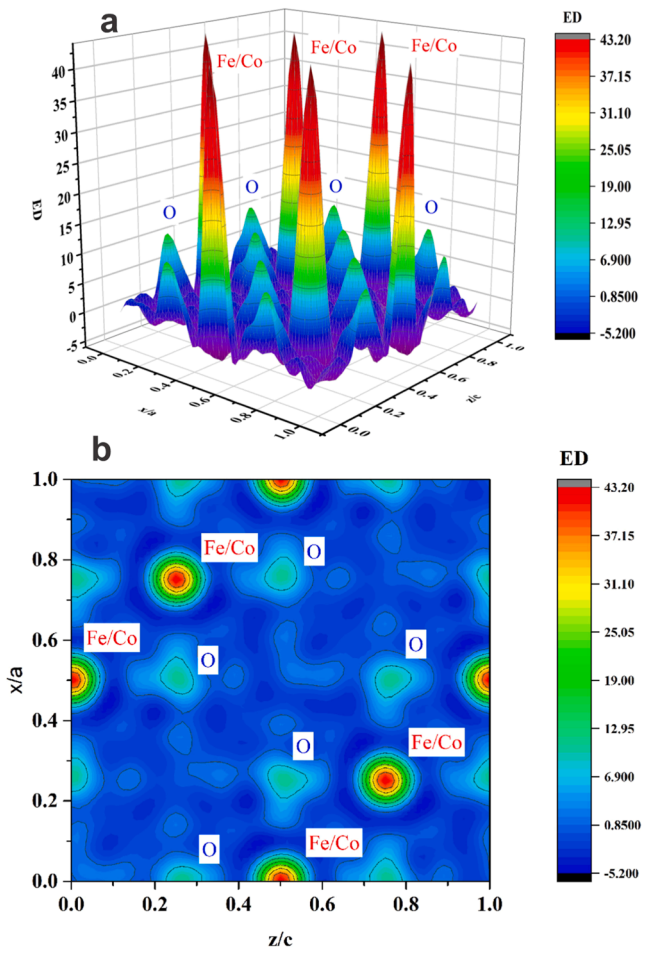

Fig. 4. Electron density maps of the $CoFe_2O_4$ structure: (a) – 3D electron density map showing the spatial distribution of atoms within the unit cell, (b) – 2D electron density map showing a planar section through the center of the cell.

FeO_6 octahedra share common vertices or edges. This leads to the formation of a spatial lattice with balanced density, contributing to the material's high mechanical and thermal stability.

Data from VESTA also show that the bond lengths for Fe–O and Co–O are 2.037 Å and 1.964 Å, respectively, and the tilt angles of the octahedral pyramids are approximately 58°. These parameters highlight the symmetry and dense packing of atoms in the crystal structure.

Cobalt ferrite crystallizes in the spinel structure AB_2O_4 (space group Fd-3m) with cations at 8a (tetrahedral, A) and 16d (octahedral, B) sites and oxygen at 32e. $CoFe_2O_4$ typically exhibits a partially inverse cation arrangement $(Fe^{3+})_{8a}[Co^{2+},Fe^{3+}]_{16d}O_4$. The inversion degree iii (fraction of Fe^{3+} on 8a) depends on synthesis/annealing conditions and governs the local M–O bond chemistry.

Electron-density (ED) maps reconstructed from the Rietveld model (GFourier) and visualized in VESTA reveal more extended and intense density channels along 16d–O bonds compared with 8a–O, indicating a higher covalent contribution in the B-sublattice. For quantitative interpretation we employ: a bond-covalency index

$$C_{Oh/Td} = \frac{\rho_{max}(16d - O)}{\rho_{max}(8a - O)},$$

site-integrated ED Q_{16d}, Q_{8a}, Q_{32e} obtained by spherical integration within fixed radii around cation and oxygen sites, and the residual-density metric $\max|\Delta\rho|$ as a consistency check. For an inverse spinel one expects $C_{Oh/Td} > 1$ and $Q_{16d} > Q_{8a}$. An increase in C_{Oh}/T_d (stronger 16d–O channels) is consistent with enhanced O(2p)–M(3d) hybridization in the B-network and typically coincides with improved agreement factors (lower R-values) when partial inversion is allowed in the refinement.

Fig. 5 shows the electron density maps for the CoO structure.

The 3D electron density map (Fig. 5a) illustrates the distribution of electrons around Co and O atoms in the CoO unit cell. Regions of high electron density are concentrated around Co^{2+} and O^{2-} ions, indicating strong interactions between them. The regular alternation of high- and low-density regions emphasizes the close packing of atoms in the crystal lattice. The map also reveals clearly defined octahedral coordination zones, where oxygen atoms surround cobalt ions.

The 2D electron density map (Fig. 5b) shows the electron density distribution in a plane passing through the center of the unit cell. The maximum density corresponds to the positions of Co^{2+} ions, while the minimum occurs in the interatomic regions. Clear Co–O bonds are visible on the map, aligned along the principal directions of the crystal lattice.

The Co–O bond length is 2.13 Å, confirming the high symmetry and structural order of the lattice. These results align with both experimental and theoretical data, validating the regular atomic arrangement in the CoO unit cell.

Cobalt(II) oxide crystallizes in a cubic (space group Fm-3 m) structure with octahedral coordination of Co^{2+} and six equivalent Co–O bonds. Electron-density (ED) maps of CoO reconstructed by GFourier are, in the ideal case, nearly isotropic around both Co and O, showing a radially symmetric decay of ρ(r) and uniform maxima along the six Co–O

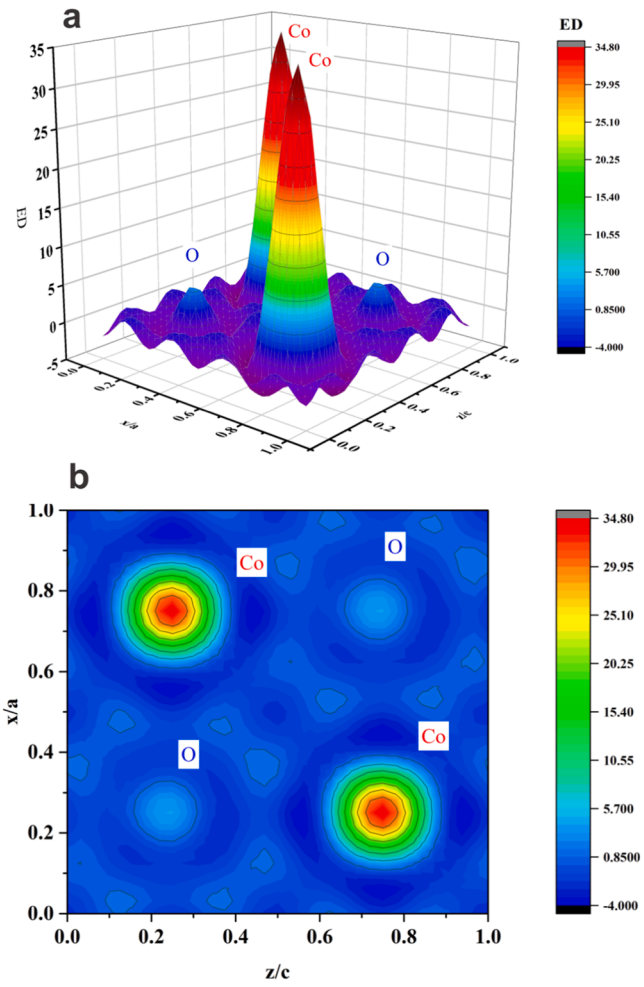

Fig. 5. Electron density maps of the CoO structure: (a) – 3D map showing the spatial distribution of atoms within the unit cell, (b) – 2D map showing a planar section through the center of the cell.

directions. Quantitatively, this appears as: equal local peaks ρ max (Co−O) in any crystallographic direction (within uncertainty); similar site-integrated densities Q_{Co} across specimens; and low max$|\Delta\rho|$ when thermal parameters (B-factors) are modeled correctly. In spinel + CoO mixtures, the CoO contribution is readily recognized by the absence of tetrahedral (Td) channels and by more compact octahedral peaks, in contrast to the extended 16d–O channels of $CoFe_2O_4$. As the CoO fraction increases, the overall ED pattern loses Td signatures and exhibits a more isotropic character.

The next step is the analysis of electron density maps of Fe_2O_3, shown in Fig. 6, which provide a detailed representation of the electron distribution around Fe^{3+} and O^{2-} ions.

The 3D electron density map (Fig. 6a) shows the spatial distribution of electron density. High density is observed around the Fe atoms, indicating their key role in the structural stability of the compound. The O atoms exhibit less intense electron density, confirming their role as anions in the crystal structure. The regular arrangement of high-density regions reflects the strict ordering of atoms within the unit cell.

The 2D map (Fig. 6b) represents a cross-section through the center of the unit cell, providing a detailed view of the electron density distribution. Maximum density is found at the Fe atom positions, emphasizing their central role in coordination, while the O atoms form a lattice with lower density in the interatomic spaces. The uniform distribution of electron density along the main x/a and z/c axes highlights the symmetry of the Fe_2O_3 structure. These maps confirm the atomic ordering

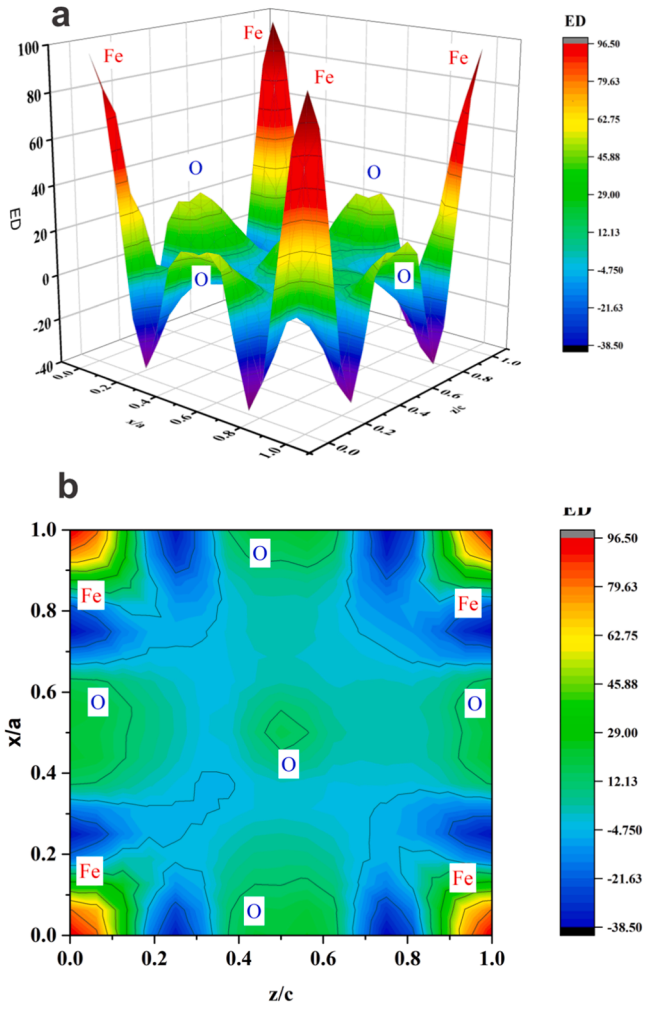

Fig. 6. Electron density maps of the Fe_2O_3 structure: (a) – 3D map showing the spatial distribution of atoms within the unit cell, (b) – 2D map showing a planar section through the center of the cell.

and underline key features of the Fe_2O_3 crystal structure.

Hematite α-Fe_2O_3 is characterized by a corundum-like structure ($P4_332$) with split rows of octahedrally coordinated Fe^{3+}. In ED maps, this produces anisotropic density ridges along the Fe−O bonds and "chains" along the octahedral network; the QFe and QO integrals are more pronounced along crystallographic directions than in cubic phases.

To turn Fourier electron-density (ED) maps (GFourier/VESTA) from descriptive visuals into a reproducible analysis, we adopt a unified set of quantitative metrics and compare them across phases and samples. For the spinel $CoFe_2O_4$, we use the octahedral-to-tetrahedral covalency index $C_{Oh/Td}=\rho_{max}(16d-O)/\rho_{max}(8a-O)$ and the site-integrated ED values Q_{8a}, Q_{16d}, Q_{32e} obtained by spherical integration around cation and oxygen positions. For non-spinel components we analogously report Q_{Co}, Q_{Fe}, Q_O (CoO and α-Fe_2O_3). Model quality and internal consistency are monitored by the maximum residual density max$|\Delta\rho|$. In addition, line profiles ρ(r) along characteristic bonds provide ρ_{max} and a half-width as a measure of the spatial extent of density "channels." With these metrics, phases and samples can be compared directly.

Within spinel $CoFe_2O_4$ one typically finds $C_{Oh/Td} > 1$ and $Q_{16d} > Q_{8a}$, reflecting a stronger covalent component and enhanced O(2p)–*M*(3*d*) hybridization in the B-sublattice (octahedral 16d sites). As $C_{Oh/Td}$ and Q_{16d} increase, the 16d–O channels become more extended, indicating a structurally more connected B-network. In CoO (NaCl type) the ED is more isotropic around Co and O; the absence of tetrahedral channels is a clear fingerprint of this phase. The contribution of α-Fe_2O_3 (corundum) appears as anisotropic octahedral "ridges" and distinct Q integrals. Correlating these ED metrics with phase fractions from Rietveld refinement and with the electrical response (resistivity ρ, Arrhenius activation energy E_a) yields a coherent picture: samples with more developed 16d–O channels (larger $C_{Oh/Td}$, higher Q_{16d}) generally exhibit lower ρ and more pronounced thermally activated conduction along the B-sublattice; increasing CoO content isotropizes the ED landscape and weakens spinel Td/Oh signatures; the α-Fe_2O_3 contribution is distinguishable by its topology and Q values. This framework renders the GFourier/VESTA section quantitative and directly links charge distribution to crystal chemistry and the electronic response in $CoFe_2O_4$–CoO– α-Fe_2O_3 composites.

As a result of the conducted studies, it was established that the obtained sample is a multicomponent system with a pronounced crystalline structure, including $CoFe_2O_4$, Fe_2O_3, and CoO domains. The formation of these phases is determined by the chosen synthesis conditions and explains the observed combination of magnetic, structural, and physical properties of the material. The spinel $CoFe_2O_4$ is widely reported to possess high magnetocrystalline anisotropy arising from Co^{2+} at octahedral sites (strong spin–orbit coupling) [51,52]; in our multiphase samples, minor Fe_2O_3 and CoO detected by XRD could potentially affect thermal stability and mechanical behavior via interfacial phenomena, but these effects were not evaluated here and we refrain from making claims.

Comprehensive analysis confirmed that the mutual dMistribution of phases and their structural parameters are consistent with theoretical predictions, validating the promise of this approach for obtaining materials with improved characteristics. These results lay the foundation for further optimization of the synthesis technology aimed at targeted control of phase composition and material properties.

4.4. Investigation of the synthesized cobalt ferrites using TEM-EDX analysis

To gain a detailed understanding of the domain morphology and to clarify the relationship between stoichiometric composition and phase characteristics of the samples, an in-depth study of $CoFe_2O_4$ samples with varying stoichiometry was conducted using TEM-EDX analysis and high-resolution transmission electron microscopy (HR-TEM).

Fig. 7 shows the results of the study of sample No. 1, including the TEM image (Fig. 7a) and the elemental analysis spectrum obtained by

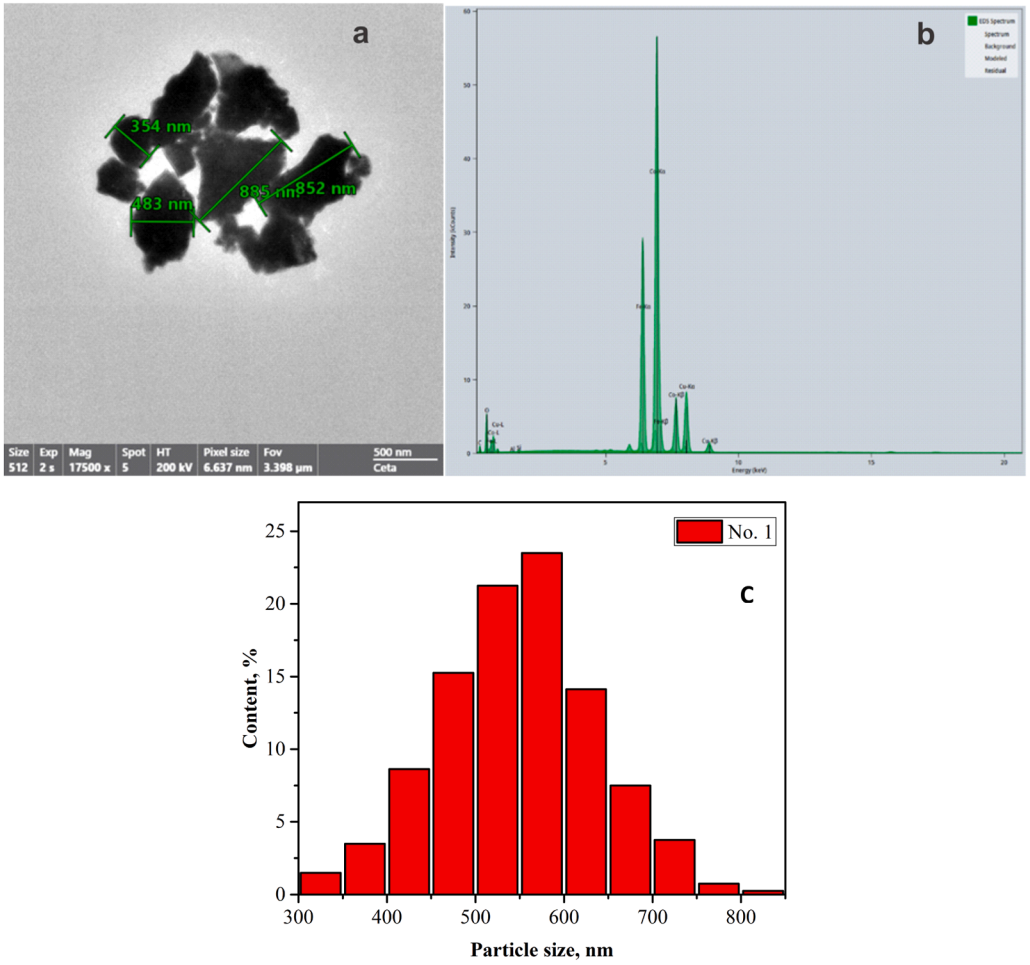

Fig. 7. TEM image (a), EDX spectrum (b) and particle size distribution histogram (c) for sample No. 1 ($Co_3FeO_{1.2}$).

energy-dispersive X-ray spectroscopy (EDX) (Fig. 7b). The microstructure of sample No. 1 (Fig. 7a) is characterized by the presence of fine-dispersed particles distributed throughout the material. The particles are predominantly irregular in shape. The DLS-based size distribution spans 300–900 nm with a mean size of ~550 nm and a peak in the 550–600 nm bin (Fig. 7c). An uneven distribution of particles is observed, which may be associated with the characteristics of the grinding process. The morphology of the particles indicates their polycrystalline nature, confirmed by the presence of grain boundaries. The spectrum and EDX analysis results (Fig. 7b) confirm the presence of the main sample elements: cobalt (Co), iron (Fe), and oxygen (O), as well as impurities of aluminum (Al) and silicon (Si). The elemental composition of sample No. 1 is distributed as follows: cobalt (Co): 60.9 at%, iron (Fe): 24.3 at%, oxygen (O): 14.537 at%, aluminum (Al): 0.140 wt% and silicon (Si): 0.123 wt%. The content of the main elements, according to the EDX analysis data (Table 5), confirms the data obtained by XRF analysis (Table 3). The high cobalt content and relatively low iron content indicate a deviation from the theoretical stoichiometric ratio for $CoFe_2O_4$. This also confirms the XRF analysis results and emphasizes the formation of a cobalt-rich compound. The presence of Al and Si impurities, despite their low concentration, may be associated with raw material contamination or synthesis process characteristics. The oxygen content confirms the formation of oxides that make up the sample structure. Thus, TEM and EDX analyses show that sample No. 1 consists of fine oxide particles with a polycrystalline structure and contains an excess of cobalt, corresponding to a deviation from stoichiometry. These data are important for understanding the influence of composition on the material's properties and its further application.

Table 5
EDX analysis data of samples with different stoichiometric compositions.

	No.1-$Co_3FeO_{1.2}$	No.2-$CoFeO_{2.5}$	No.3-$CoFe_2O_4$	No.4-$CoFe_{2.8}O_4$
Comp.	Content, atomic fraction, %			
O	14.537	9.464	6.768	5.573
Al	0.140	0.138	0.126	0.129
Si	0.123	0.118	0.106	0.098
Fe	24.3	44.1	63.2	70.9
Co	60.9	46.2	29.8	23.3

Fig. 8 shows the results of the study of sample No. 2, including the TEM image (Fig. 8a) and the EDX spectrum (Fig. 8b).

In the TEM image (Fig. 8a), the microstructure of sample No. 2 is characterized by a more uniform distribution of particles compared to sample No. 1. The particles are predominantly irregular in shape. The DLS-based size distribution spans 251–802 nm with a mean size of ~482 nm and a peak in the 475–525 nm bin (Fig. 8c). Partial agglomeration of particles is observed, which may be associated with the specifics of the grinding process. The polycrystalline nature of the particles is confirmed by the presence of grain boundaries, indicating their complex internal structure. The spectrum (Fig. 8b) and the results of the EDX analysis (Table 5) confirm the presence of the main elements, with their content close to the XRF data presented in Table 3. The elemental composition of the $CoFeO_{2.5}$ sample is distributed as follows: Co – 46.2 at%, Fe – 44.1 at%, O – 9.464 at%, Al – 0.138 wt%, and Si – 0.118 wt%. The cobalt and iron contents are almost close to the calculated values, indicating a more balanced ratio between components

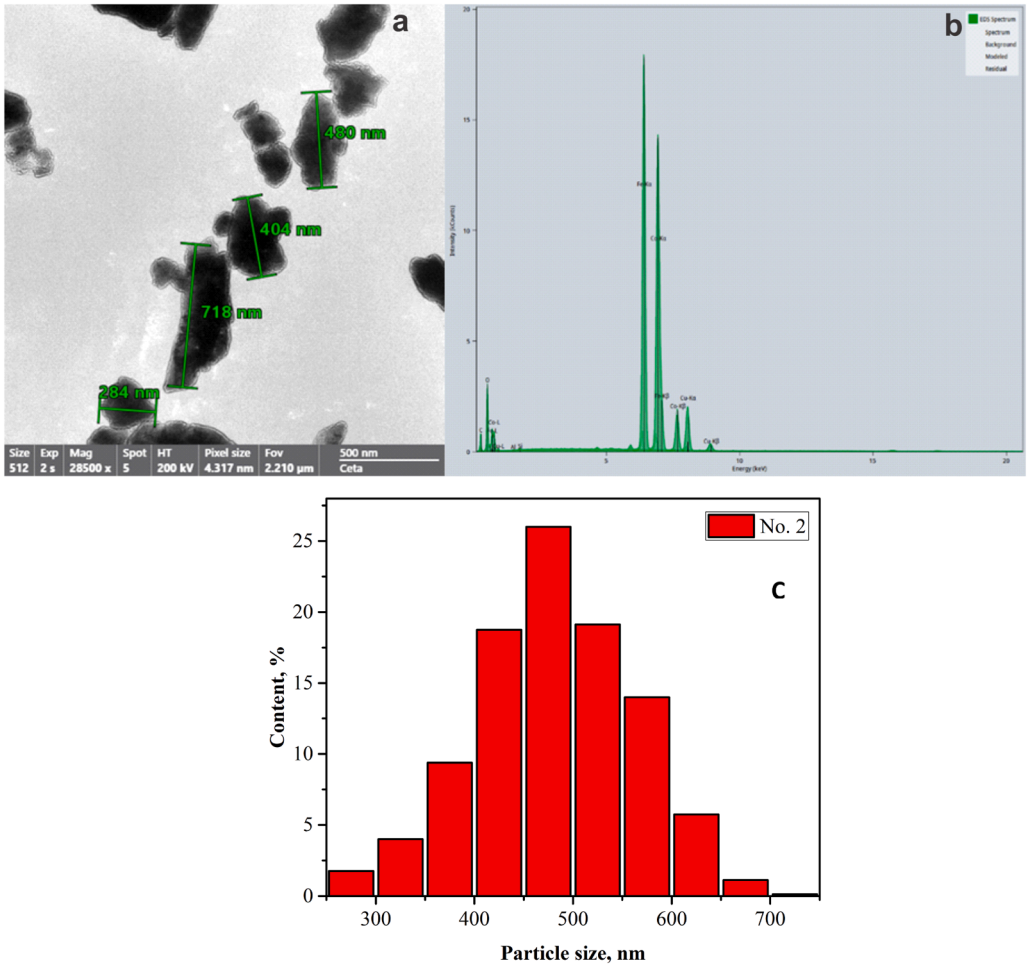

Fig. 8. TEM image (a), EDX spectrum (b) and particle size distribution histogram (c) for sample sample No. 2 ($CoFeO_{2.5}$).

compared to sample No. 1.

Fig. 9 shows the TEM and EDX analysis results for sample No. 3.

The microstructure of sample No. 3 is represented by larger and more uniformly distributed particles compared to the previous samples. The particles are predominantly irregular in shape. The DLS-based size distribution spans 298–649 nm with a mean size of ~409 nm and a peak in the 375–425 nm bin (Fig. 9c). This confirms a high degree of crystallinity of the sample. The microstructure features an ordered structure with clearly defined grain boundaries, indicating the presence of a well-developed crystal lattice.

The spectrum (Fig. 9b) and the results of the EDX analysis (Table 5) confirm the presence of three main elements in the sample composition: cobalt (Co), iron (Fe), and oxygen (O). The content of these elements in sample No. 3 is distributed as follows: Co – 29.8 at%, Fe – 63.2 at%, O – 6.768 at%, Al – 0.126 wt%, and Si – 0.106 wt%.

The high iron content and the lower cobalt content correspond to the stoichiometric composition of $CoFe_2O_4$, confirming that the sample's composition matches the theoretical values for this compound. A small amount of aluminum and silicon impurities is present in the sample. Finally, Fig. 10 presents the TEM and EDX analysis results for sample No. 4.

The microstructure of sample No. 4 exhibits coarser particle dispersion compared to the previous samples. The particles are predominantly irregular in shape. The DLS-based size distribution spans 402–1193 nm with a mean size of ~881 nm and a peak in the 880–900 nm bin (Fig. 10c). The sample exhibits less pronounced morphological homogeneity, with the presence of aggregates, which may be related to the increased iron content. The formation of these aggregates is likely due to differences in crystal growth rates and phase transitions associated with the increased iron content.

At the same time, individual particles show a highly crystalline structure with well-defined grain boundaries, confirming the presence of a stable oxide phase.

The spectrum (Fig. 10b) and the results of the EDX analysis (Table 5) show that the composition of sample No. 4 includes the following elements: Co – 23.3 at%, Fe – 70.9 at%, O – 5.573 at%, Al – 0.129 wt%, and Si – 0.098 wt%.

The significant increase in iron (Fe) content compared to cobalt (Co) confirms a deviation from the stoichiometric norm for $CoFe_2O_4$ and a shift toward more iron-rich compounds, which agrees with the XRF analysis data.

This may indicate that as the iron content increases, the sample structure becomes more saturated with iron oxide, which also affects the particle morphology and their agglomeration. A small amount of aluminum and silicon impurities is also present in the sample.

The results of studies on samples with different stoichiometric compositions, performed using TEM and EDX methods in combination with XRF data, allow several conclusions to be drawn about the relationship between microstructure, elemental composition, and phase characteristics of these materials.

The microstructure of the samples analyzed by TEM showed that with an increase in iron content in the samples (from No. 1 to No. 4), the particle size increases, as well as a tendency toward agglomeration and uneven particle distribution is observed. Sample No. 3 was characterized by the most uniformly distributed particles with a well-defined polycrystalline structure. However, samples No. 1 and No. 2 showed more

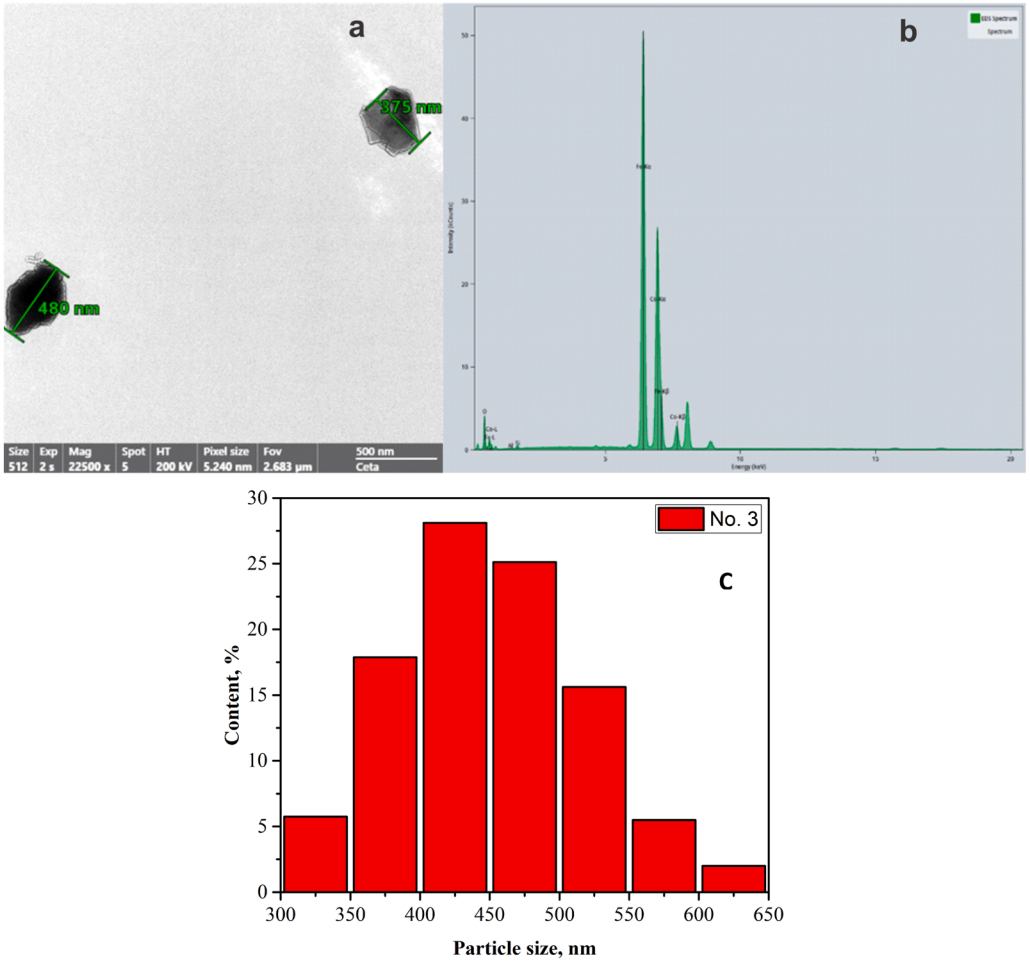

Fig. 9. TEM image (a), EDX spectrum (b) and particle size distribution histogram (c) for sample No. 3 ($CoFe_2O_4$).

pronounced deviation from stoichiometry, which also affected their microstructure, manifesting in less homogeneous particles.

EDX analysis confirmed the composition of all samples, with sample No. 1 exhibiting an excess of cobalt relative to iron, consistent with its deviation from ideal stoichiometry. In contrast, samples No. 2 and No. 3 had balanced cobalt and iron contents, closer to the theoretical composition. Sample No. 4, on the other hand, showed a high iron content, which was also confirmed by the XRF results.

Comparison of the XRF and EDX data showed that samples with different stoichiometric compositions have similar main components — cobalt, iron, and oxygen — but their ratios vary depending on the stoichiometry. Sample No. 3 exhibited the purest phase structure, while the oxygen content varied in the other samples, which may be due to synthesis conditions and the presence of impurities.

Based on all the obtained data, it can be concluded that by changing the ratio of cobalt and iron in $CoFe_2O_4$ samples, it is possible to control their phase composition, microstructure, and properties.

For a more detailed structural analysis, sample No. 3 was selected for study using HR-TEM, as it has the highest phase content and is the closest to the theoretical composition.

The high degree of crystallinity of this sample allows for a more accurate study of its nanostructure and phase characteristics at the atomic level.

Fig. 11 presents the HR-TEM image of sample No. 3, chosen for high-resolution analysis due to its most balanced composition corresponding to the theoretical stoichiometry and the high content of the target phase, as previously confirmed by XRD and XRF data.

The HR-TEM image (Fig. 11) demonstrates a clearly defined crystal lattice with periodically repeating atomic planes. The interplanar spacing measured for the crystals of the main $CoFe_2O_4$ phase is $d = 2.53$ Å, which corresponds to the (311) plane of the spinel structure, previously confirmed by XRD data (JCPDS No 96–153–3164).

In addition, domains of Fe_2O_3 and CoO phases were detected on the HR-TEM image, which form as a result of slight stoichiometric deviation and local chemical changes during the synthesis process. For the Fe_2O_3 phase crystals, the interplanar spacing is $d = 2.70$ Å, corresponding to the (012) plane of hematite (JCPDS No 96–230–0618). For the CoO crystals, the interplanar spacing was measured as $d = 2.46$ Å, which corresponds to the (111) plane of the cubic structure (JCPDS No 96–153–3088).

HR-TEM images also reveal the presence of oriented domains with different crystallographic orientations. These domains are highly ordered regions separated by distinct boundaries. The domain boundaries may be associated with local stresses arising during crystal growth.

The domains of the main $CoFe_2O_4$ phase exhibit a stable structure, with the growth direction corresponding to the dominant (311) and (400) planes, which is consistent with the XRD data. The domains of the Fe_2O_3 and CoO phases are smaller in size and may result from incomplete reaction or thermal processing. These phases are localized near the boundaries, which may also indicate heterogeneity in the growth processes.

HR-TEM lattice-fringe analysis (via FFT) indicates an average crystallite size of ~24 nm.

HR-TEM data confirm that the composition and structure of sample No. 3, determined using XRF and XRD, are consistent with the nanostructure revealed by high-resolution electron microscopy. HR-TEM

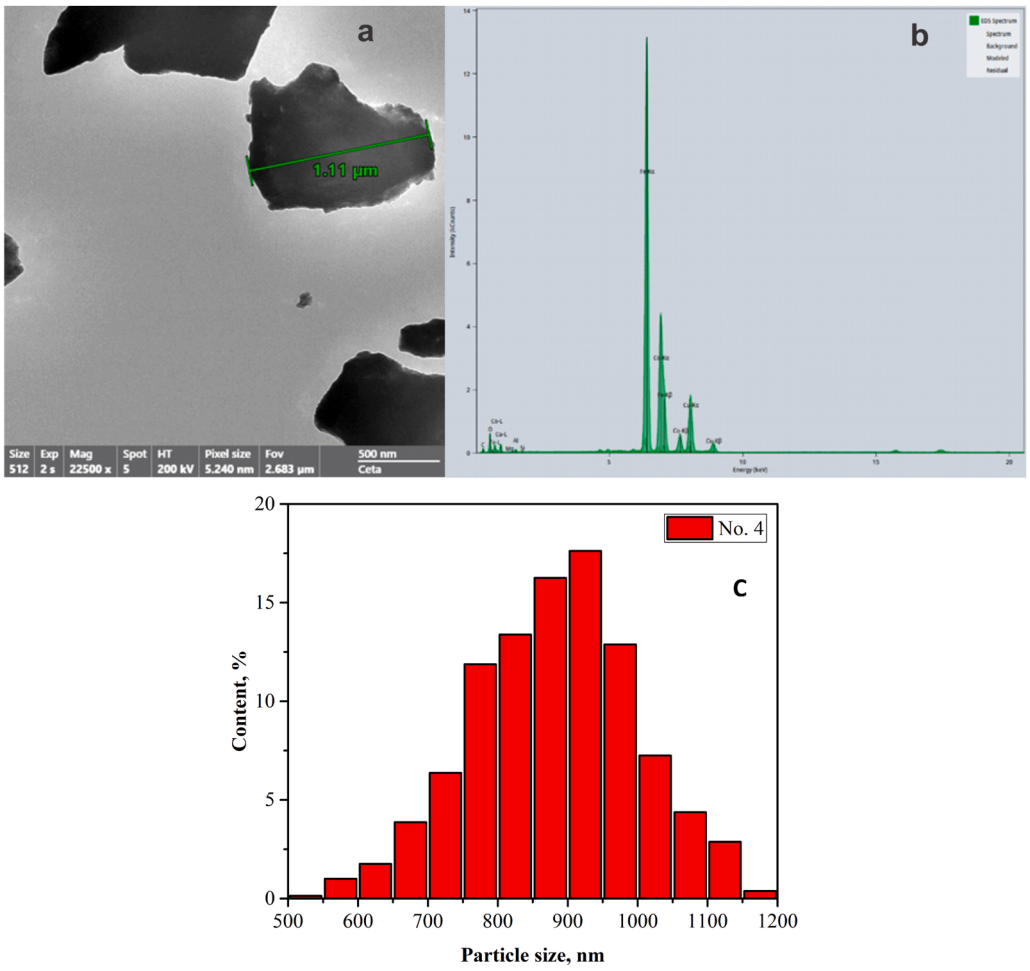

Fig. 10. TEM image (a), EDX spectrum (b) and particle size distribution histogram (c) for sample No. 4 ($CoFe_{2.8}O_4$).

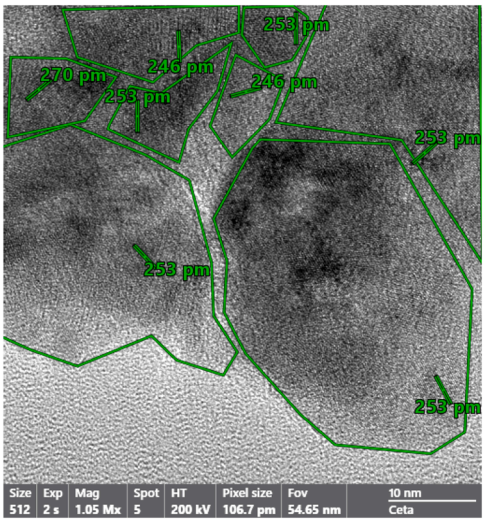

Fig. 11. HR-TEM image of sample No. 3-$CoFe_2O_4$.

analysis showed that the $CoFe_2O_4$ sample is characterized by a high degree of crystallinity and the presence of oriented domains of the main phase and secondary phases (Fe_2O_3 and CoO). The measured interplanar spacings (d = 2.53 Å for $CoFe_2O_4$, d = 2.70 Å for Fe_2O_3, d = 2.46 Å for CoO) confirmed the crystalline nature of the sample. Domains with sharp boundaries and low defect content indicate the material's potential for use in magnetic and oxide devices requiring phase purity and stability.

4.5. Microstructural and microchemical analysis (HAADF-STEM/EDX)

HAADF-STEM/EDX was performed on the representative sample No. 3 (nominal spinel stoichiometry $CoFe_2O_4$) to assess microchemical homogeneity (Fig. 12).

The HAADF image (Fig. 12a) shows submicron, near-isometric particles with smooth internal Z-contrast; slight edge brightening is attributed to thickness variations typical of HAADF. Elemental maps of O–K, Fe–K, and Co–K (Fig. 12c–e) reveal spatial co-localization of Co and Fe across entire grains without Co- or Fe-enriched shells/cores, while oxygen follows the particle morphology. The carbon map (Fig. 12b) displays a weak, discontinuous signal outside the grains and is interpreted as background from the support/adsorbates. Point spectra collected from two intragrain positions (Area #1 and Area #2; Fig. 12g, h) exhibit identical characteristic lines (O–K, Fe–Kα/β, Co–Kα/β) with similar relative intensities; no foreign elements were detected above the EDX detection limit under these conditions (~0.5–1 at%). Thus, at the $\sim 10^2$ nm scale, sample No. 3 exhibits a uniform elemental distribution with no evidence of micro-segregation.

These findings agree with the diffraction analysis: multiphase Rietveld refinement indicates dominance of the $CoFe_2O_4$ spinel with only minor secondary oxides, consistent with the absence of Co- or Fe-rich domains in the maps. Electrical measurements likewise show no signature of composition-driven inhomogeneity; the high, reproducible bulk resistivity ($\approx 7.8 \times 10^7$ Ω cm) suggests transport governed primarily by

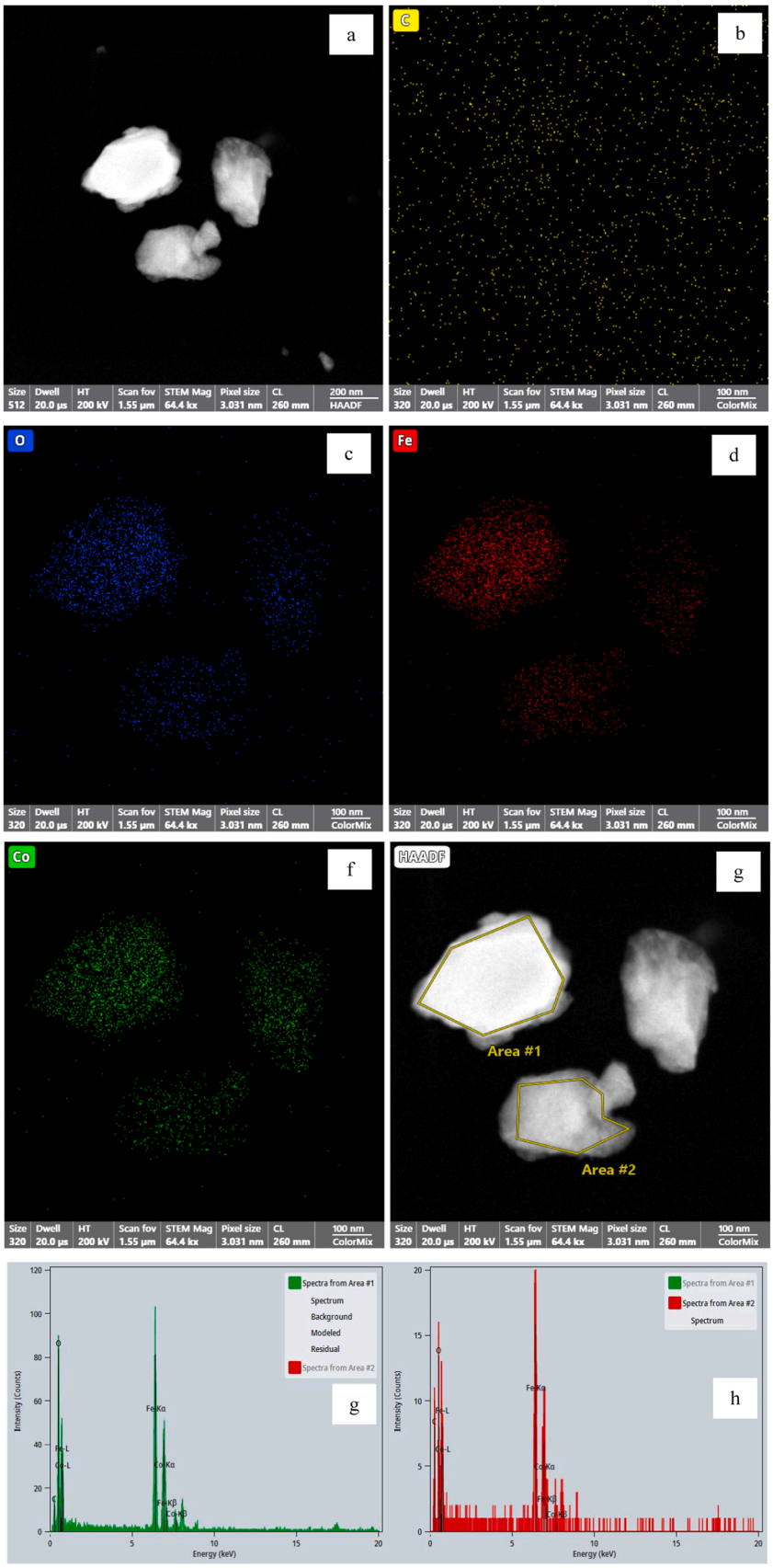

Fig. 12. HAADF-STEM/EDX mapping of sample No. 3 ($CoFe_2O_4$). (a) HAADF-STEM image of particles; (b) carbon distribution map; (c) O–K map; (d) Fe–K map; (e) Co–K map; (f) HAADF image with marked analysis areas (Area #1, Area #2); (g) EDX spectrum from Area #1 with fitting; (h) EDX spectrum from Area #2.

grain-boundary/defect contributions rather than local stoichiometry fluctuations. We note that quantitative STEM-EDX from point spectra can be affected by thickness, absorption, and particle geometry; Accordingly, conclusions focus on elemental co-localization in maps and relative line-intensity comparisons within the same grain—a conservative and reliable criterion at this spatial resolution. Overall, the HAADF-STEM/EDX results confirm the microchemical homogeneity of sample no. 3 ($CoFe_2O_4$) and are fully consistent with the XRD and electrical data.

4.6. Investigation of the electrical resistivity of the obtained cobalt ferrites using the four-point probe method

To evaluate the electrical properties of synthesized $CoFe_2O_4$ samples with various stoichiometries, the specific resistivity (ρ) was measured using the Van der Pauw four-point probe method with the ST2258C device. The samples, in the form of pressed pellets with a diameter of 10 mm and a thickness of 10 mm, were pre-cleaned from contaminants, and their surfaces were leveled to ensure reliable contact with the probes. Measurements were carried out at room temperature (25°C) with current values of 10 μA, 100 μA, 1 mA, etc. The specific resistivity was calculated using the formula:

$$\rho = Rs \cdot t,$$

where Rs is the sheet resistance, and t is the thickness of the sample. The Rs value was automatically determined by the device based on the measured voltage (V) and current (I) using the formula:

$$Rs = 4.532 \cdot V/I$$

To visualize the dependence of the resistivity of $CoFe_2O_4$ samples on the percentage ratio of CoO and Fe_2O_3, the oxide fractions in each sample were calculated based on their stoichiometric formulas. The results are presented in Table 6 below and subsequently converted into Fig. 13.

The results clearly demonstrate the significant influence of stoichiometry on the electrical properties. Sample No. 3 exhibited the highest resistivity (7.8×10^7 Ω·cm), which is attributed to its high crystallinity and the predominance of the spinel phase, acting as barriers to charge transport. Samples No. 1 and No. 4, which contained excess CoO and Fe_2O_3, respectively, showed intermediate resistivity values (2.6×10^6 and 4.3×10^7 Ω·cm), likely due to the presence of secondary phases that disrupt the electronic structure. In contrast, pure oxides of CoO and Fe_2O_3 demonstrated substantially lower resistivities (10^5 and 10^2 Ω·cm, respectively), thereby confirming the critical role of phase composition in determining the electrical behavior.

Quantitatively, increasing spinel phase purity—i.e., reducing CoO/Fe_2O_3 fractions by XRD–Rietveld with corroborating XRF/EDX—correlates with higher and more reproducible bulk resistivity. The highest ρ is observed for sample No. 3, where $CoFe_2O_4$ predominates; excess CoO or Fe_2O_3 introduces additional grain-boundary barriers/traps, broadening the spread and lowering transport uniformity. This trend is consistent with STEM-EDX mapping (uniform Co/Fe/O) and multiphase refinement indicating spinel dominance.

Fig. 13 illustrates a nonlinear dependence of resistivity on the percentage ratio of CoO and Fe_2O_3. The maximum resistivity is observed at the stoichiometric ratio of 1:2 (Sample No. 3 – $CoFe_2O_4$), while the minimum corresponds to the pure oxides CoO and Fe_2O_3. This behavior is attributed to the material's electronic structure and the presence of impurity phases.

Table 6
Molar ratios and results of specific resistivity measurements for $CoFe_2O_4$ samples.

Sample No.	Composition	CoO, %	Fe_2O_3, %	Electrical Resistivity, Ω·cm
CoO	CoO	100	0	2.0×10^5
No.1	$Co_3FeO_{1.2}$	85.7	14.3	2.6×10^6
No.2	$CoFeO_{2.5}$	66.7	33.3	3.0×10^7
No.3	$CoFe_2O_4$	33.3	66.7	7.8×10^7
No.4	$CoFe_{2.8}O_4$	14.3	85.7	4.3×10^7
Fe_2O_3	Fe_2O_3	0	100	5.0×10^2

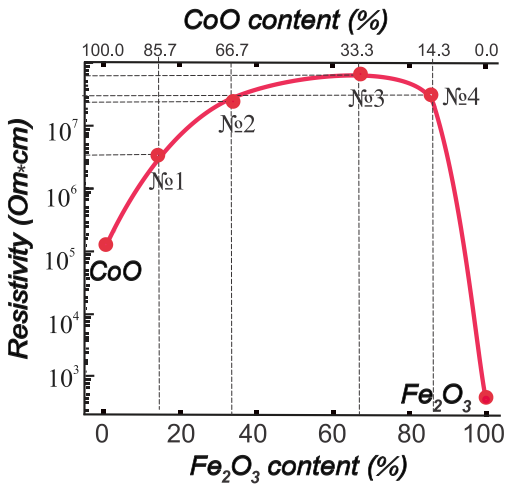

Fig. 13. Dependence of resistivity on the composition of $CoFe_2O_4$ samples.

In the spinel structure of $CoFe_2O_4$, Fe^{3+} ions occupy octahedral positions, whereas Co^{2+} ions are located in tetrahedral sites. Oxygen ions (O^{2-}) form strong covalent bonds with the metals, trapping electrons and creating localized electronic states. This leads to an increase in the band gap (E_g) and limits charge carrier mobility.

Sample No. 3 ($CoFe_2O_4$, 33.3 % CoO / 66.7 % Fe_2O_3) has an ideal spinel structure with an ordered arrangement of Fe^{3+} and Co^{2+} ions. The absence of impurities results in a high resistivity (7.8×10^7 Ω·cm) due to the increased band gap.

In Samples No. 1 (85.7 % CoO) and No. 4 (85.7 % Fe_2O_3), the excess CoO or Fe_2O_3 disturbs the crystal lattice, leading to the formation of secondary phases. These phases introduce additional energy levels into the band gap, facilitating electron tunneling. However, the resistivity remains high (2.6×10^6 and 4.3×10^7 Ω·cm, respectively) due to structural defects that scatter charge carriers.

Sample No. 2 (66.7 % CoO / 33.3 % Fe_2O_3) has an intermediate composition with partial preservation of the spinel structure. The presence of defects and CoO impurities reduces the band gap (E_g), leading to a resistivity of 3.0×10^7 Ω·cm.

This behavior is not observed in pure oxides such as Fe_2O_3 (100 % Fe_2O_3) and CoO (100 %). CoO has a monocrystalline structure with a narrow band gap (~0.8 eV), which allows electrons to overcome Eg more easily, explaining its low resistivity (2.0×10^5 Ω·cm). On the other hand, Fe_2O_3 (100 % Fe_2O_3), which corresponds to hematite (α-Fe_2O_3), has a band gap of ~2.2 eV. However, due to a high density of states in the valence band and impurity conductivity, the resistivity is the lowest (5.0×10^2 Ω·cm).

Thus, different stoichiometric compositions lead to the formation of various impurity phases of CoO and Fe_2O_3 in the samples. These create grain boundaries, increasing electron scattering. They also form regions with different band gap widths, which disrupts the uniformity of charge transport. In addition, they introduce lattice defects (oxygen vacancies, interstitial ions), which act as traps for charge carriers.

To place our room-temperature resistivity in context, we compiled a benchmark of $CoFe_2O_4$ prepared by different wet-chemistry routes (co-precipitation, hydrothermal, sol–gel; Table 7, refs. [53–57]). Reported values for polycrystalline $CoFe_2O_4$ span ~10^5–10^8 Ω·cm at RT, reflecting strong sensitivity to synthesis route, grain size and porosity, cation inversion/ordering, point-defect concentrations (Fe^{2+}/oxygen-vacancy pairs), and possible dopants. Representative undoped systems produced

Table 7
Electrical resistivity ρ (Ω·cm) of $CoFe_2O_4$: comparative data across synthesis methods.

Synthesis Method / Composition / Reference	Temperature / Condition	Resistivity ρ (Ω·cm)
Co-precipitation / $Ni_{0.7}Cu_{0.1}Zn_{0.2}La_xFe_{2-x}O_4$ / [53]	RT (room temperature)	≈ 2.0621×10^7
Hydrothermal / $CoLi_xCd_xFe_{2-2x}O_4$ / [54]	RT	≈ 7.3×10^7
Sol–gel / $CoFe_2O_4$ / [55]	30 °C – 700 °C	≈ 5.1×10^7
Sol–gel / $CoFe_2O_4$ / [56]	при нагреве до 95 °C	≈ 5.1×10^6
Co-precipitation / $CoFe_2O_4$ / [57]	RT	≈ 1.44×10^8

by sol–gel routes typically show ρ ≈ 10^6–10^7 Ω·cm, while co-precipitated powders often fall in the 10^5–10^6 Ω·cm range; the highest values (≳ 10^8 Ω·cm) are uncommon and usually associated with specific chemistries and/or post-treatments [53–57].

Against this background, our Large Solar Furnace (LSF) sample exhibits ρ = 7.8×10^7 Ω·cm (RT), which lies within the upper envelope of literature data for undoped $CoFe_2O_4$ and exceeds most values reported for conventional co-precipitation and many sol–gel syntheses (Table 7). We ascribe this elevated resistivity to the defect/structure state attained under rapid, high-flux solar heating: the short thermal cycle limits reduction-driven Fe^{2+} formation and oxygen-vacancy population and promotes insulating grain-boundary barriers, consistent with our structural and microstructural characterization (see Sections …). This comparison underscores the advantage of the solar-thermal route for obtaining highly resistive $CoFe_2O_4$ without complex post-processing.

4.7. First-principles density functional theory (DFT) calculations electronic and band structure of obtained cobalt ferrite synthesized in the large solar furnace

To place the electrical behavior in a microscopic context, we computed band structures and densities of states (DOS) for CoO and $CoFe_2O_4$ (Fig. 14). Calculations were performed with the Vienna Ab initio Simulation Package (VASP; PAW, PBE), using a collinear spin setup; test spin–orbit–coupled runs on representative structures changed the band gap by < 0.05 eV and did not alter the conclusions. The GGA-PBE functional was augmented by on-site Hubbard corrections in the Dudarev formalism (GGA+*U*). Projector-augmented wave (PAW) potentials were used for Co, Fe and O (valence: Co $3d^7 4s^2$, Fe $3d^6 4s^2$, O $2s^2 2p^4$). A plane-wave cutoff of 520 eV ensured convergence; tests at 450/520/600 eV changed the total energy by < 2 meV per atom and left the gap stable. Brillouin-zone integration used Γ-centered Monkhorst–Pack meshes of 4 × 4 × 4 for structural relaxations (56-atom inverse-spinel cell) and 6 × 6 × 6 for final electronic/DOS runs. Self-consistent cycles employed Gaussian smearing σ = 0.05 eV (varying σ between 0.02–0.10 eV did not affect gap opening); DOS was refined with the tetrahedron method with Blöchl corrections. Convergence thresholds were 10^{-6} eV in total energy, ≤ 0.01 eV $Å^{-1}$ in residual forces, and ≤ 0.2 GPa in residual stress; lattice parameter and internal coordinates were relaxed until all criteria were met. Effective on-site interactions were $U_{eff(Fe\text{-}3d)}$= 4.0 eV and $U_{eff(Co\text{-}3d)}$= 3.3 eV—values commonly used for Co–Fe spinels; varying U by ±0.5 eV changed the band gap by ~0.1–0.2 eV without altering the magnetic ground state.

The band structure calculated without U (Fig. 14a; "GGA only") illustrates the well-known GGA failure in correlated oxides, yielding spurious metallicity or an unrealistically small gap due to underestimated on-site correlations on Co-3d orbitals. Introducing U (Fig. 14b; GGA+*U*) opens an indirect gap of ~0.99 eV. Near the Fermi level, relatively flat bands originate from localized Co-3d states, whereas deeper dispersive bands derive from O-2p hybridized with Co-3d. The DOS corroborates this picture, showing a clean gap with a valence band dominated by hybridized O-2p/Co-3d states and a conduction band comprised mainly of unoccupied Co-3d states—consistent with the

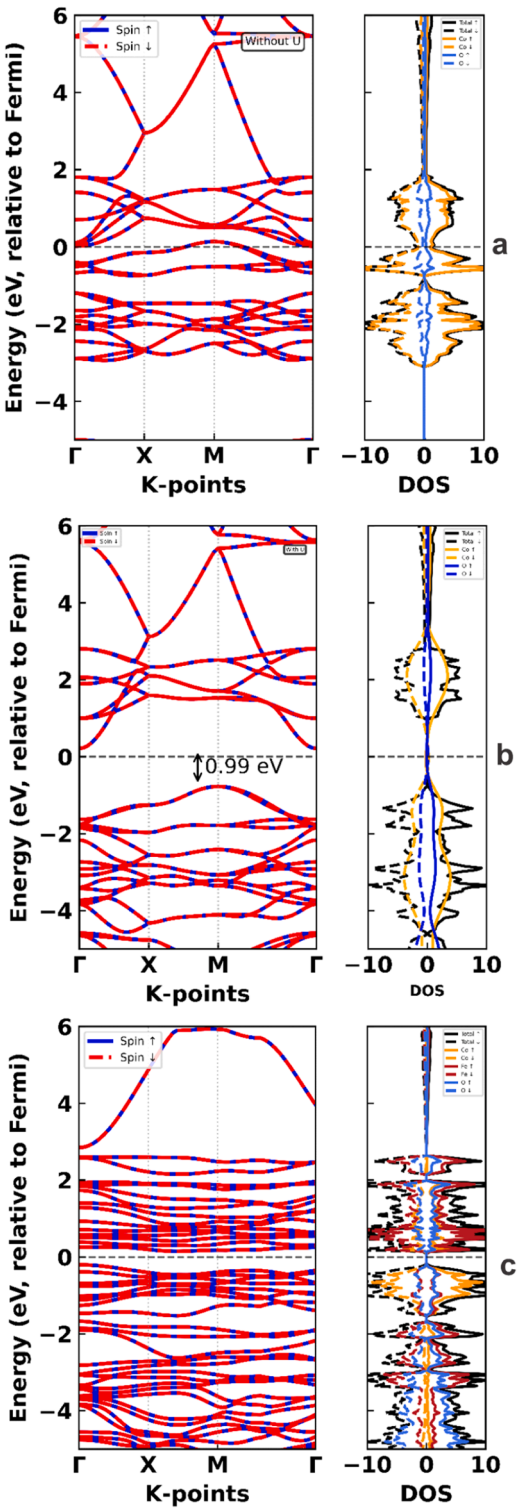

Fig. 14. Electronic band structures and density of states (DOS) plots: a) - CoO calculated without the Hubbard U correction (GGA only). b) - CoO calculated with the Hubbard U correction (GGA+*U*), showing an indirect band gap of 0.99 eV. c) - $CoFe_2O_4$ calculated within the GGA+*U* approximation, exhibiting a larger spin-polarized band gap and distinct contributions from Co, Fe, and O orbitals.

Mott-insulating character of CoO.Cobalt ferrite was modeled as an inverse spinel (space group

Fd-3m) with full inversion: Co^{2+} occupy octahedral B (16d) sites, while Fe^{3+} populate both tetrahedral A (8a) and octahedral B (16d)

sublattices. The magnetic order is ferrimagnetic with antiparallel A/B sublattices; initial collinear moments (+5 μB on Fe^{3+}(A), −5 μB on Fe^{3+}(B), −3 μB on Co^{2+}(B)) relax to a ferrimagnetic ground state with a non-zero net magnetization per formula unit, in agreement with the expected inverse-spinel chemistry. Within GGA+*U* the spin-polarized band structure (Fig. 14c) exhibits an insulating gap $E_g \approx 1.5–1.8$ eV (depending on U within the tested range). Orbital-projected DOS indicates pronounced O-2p–(Fe,Co)-3d hybridization: the valence-band top is largely O-2p mixed with transition-metal t_2g, while the conduction-band bottom is predominantly (Fe,Co)-3d e_g centered on octahedral B sites. The stronger hybridization at B sites aligns with their dominant role in setting carrier barriers in the inverse spinel.

In contrast to CoO, whose insulating state arises mainly from on-site 3d correlations of Co (Mott-type), $CoFe_2O_4$ displays a more complex, charge-transfer-like insulating behavior due to the participation of both Co- and Fe-3d states and their hybridization with O-2p. The spin-resolved bands and DOS of $CoFe_2O_4$ reveal a robust ferrimagnetic insulator, not an antiferromagnet. The GGA+*U* gap (1.5–1.8 eV) places the Fermi level inside a clean forbidden region with no in-gap states in the stoichiometric model, which is consistent with the measured high room-temperature resistivity $\rho = 7.8 \times 10^7$ Ω·cm. Combined with the rapid, high-flux solar thermal cycle, this intrinsic electronic structure limits reduction-driven Fe^{2+} formation and oxygen-vacancy concentration and promotes insulating grain-boundary barriers, thereby suppressing small-polaron hopping pathways. Control tests (denser k-mesh 5 ×5 ×5 for relaxations, σ variation, and a slight reduction of inversion degree to $x \approx 0.8$) preserved the ferrimagnetic insulating state and left E_g changes within numerical uncertainty, supporting the robustness of these conclusions.

4.8. Comparison of the parameters of cobalt ferrite synthesized in the large solar furnace with those obtained by other synthesis methods

Comparative analysis of the parameters of cobalt ferrite synthesized in the Big Solar Furnace with materials obtained by traditional methods (hydrothermal synthesis, sol-gel, co-precipitation, microemulsion method, solid-state sintering) revealed significant technological and functional advantages of the solar-thermal approach (Table 8). The key comparison criteria included phase purity, particle size, energy efficiency, structural perfection, and electrophysical properties.

Solar synthesis provided a record-high content of the target spinel phase $CoFe_2O_4$ (58.1 % for the 1:2 stoichiometry) with minimal secondary phases (CoO, Fe_2O_3) and no carbon or organic impurities. This is due to the high-temperature melt (>2500 °C), which ensures complete homogenization of the precursors (CoO, Fe_2O_3), and rapid quenching (10^3 °C/s), which stabilizes the high-temperature phase. At the same time, the hydrothermal method is characterized by high crystallinity, but it carries the risk of intermediate phase formation due to incomplete precursor decomposition at lower temperatures (<300 °C). The co-precipitation method, despite its simplicity, results in non-stoichiometric compositions with a high impurity content caused by the different precipitation rates of metal ions. Solid-state sintering inevitably leads to the formation of significant amounts of secondary phases due to kinetic limitations of diffusion processes. In terms of morphology, the particles synthesized by the solar method (375–480 nm after grinding) exhibited high crystallinity, as evidenced by distinct reflections in HR-TEM images. Their uniform shape approaches the ideal geometry of nanocrystals obtained by the microemulsion method, though the latter requires toxic surfactants and laborious purification. The hydrothermal and sol-gel methods produce smaller particles (10–100 nm), but they often undergo agglomeration during subsequent thermal treatment, while solid-state sintering yields large micron-sized grains with high porosity.

The energy efficiency and environmental friendliness of the solar-thermal approach are due to the use of renewable solar energy with a flux density of about 150 W/cm^2, which minimizes the carbon footprint and significantly reduces the process duration to just a few minutes. In contrast, hydrothermal and sol-gel methods require prolonged processing with high energy consumption, while solid-state sintering is characterized by the highest energy demand. Moreover, the absence of toxic solvents and surfactants in the solar method reduces the environmental burden of production.

In terms of structural and electrophysical characteristics, the BSP-derived samples demonstrated minimal defectiveness due to rapid crystallization and a minimal amount of impurities. The maximum specific resistivity value (7.8 ×10^7 Ω·cm) for the sample with an ideal spinel structure exceeds those of materials obtained by co-precipitation methods (10^4–10^6 Ω·cm) and solid-state sintering (10^6–10^8 Ω·cm). The high resistance values are attributed to localized charge carriers in a well-organized crystal structure and the minimal presence of secondary phases, which would otherwise create additional charge transport pathways.

Secondary oxides CoO and Fe_2O_3 can distort the intrinsic properties of spinel $CoFe_2O_4$ by increasing resistivity through blockage of small-polaron hopping at interphase boundaries and by weakening magnetic characteristics via the antiferromagnetic contribution of hematite and interphase exchange [69,70]. In this work, we minimized their fraction by enforcing precise Co:Fe = 1:2 batching, complete calcination, and controlled oxidative anneals, which enabled formation of the target spinel at relatively high purity [71,72]. To reveal impurities early, we used cross-validated XRD–Rietveld and local STEM-EDX; in the representative sample No. 3, mapping confirmed uniform Co/Fe/O distributions without microsegregation. This allowed a clean structure–transport comparison: sample No. 3 exhibits high, reproducible resistivity (~7.8 × 10^7 Ω·cm) dominated by grain-boundary contributions, consistent with predominant $CoFe_2O_4$ and a low fraction of secondary oxides.

From the perspective of scalability and economic efficiency, the solar approach shows excellent prospects due to the potential use of large industrial solar furnaces and the availability of raw materials (CoO, Fe_2O_3). In contrast, methods such as microemulsion, hydrothermal, and sol-gel are limited by reactor volume, the high cost of precursors, and process complexity.

Thus, solar-thermal synthesis in the Big Solar Furnace offers clear advantages in terms of phase purity, environmental sustainability, structural perfection, and functional properties. The only drawback of the method is its dependence on weather conditions, which, however, can be mitigated by integrating additional heat sources. The results of this study confirm the high potential of the solar method for industrial production of high-quality ferrites, which are promising for applications in spintronics and magnetoelectronics.

5. Conclusion

A renewable solar-thermal route at the Large Solar Furnace (LSF) is demonstrated, enabling controlled synthesis of cobalt ferrite with a clear relationship between stoichiometry, phase composition, crystal chemistry, and transport properties. Among the studied CoO:Fe_2O_3 ratios, composition No. 3 (1:2.13) proved to be the best: 58.1 wt% $CoFe_2O_4$, $\rho = 7.8 \times 10^7$ Ω·cm, and an ordered cubic spinel Fd-3m (Rietveld refinement). Profile analysis was performed in FullProf using the TCH pseudo-Voigt function, a Chebyshev background, and the Caglioti U–V–W model; preferred orientation was modeled with the March–Dollase function. The agreement factors (Rp, Rwp, Rexp, χ^2) are within acceptable limits, and Δ2θ is small. The extracted microstructural parameters (D, ε) are consistent with HR-TEM.

TEM for sample No. 3 shows a more compact, less agglomerated morphology compared to non-stoichiometric samples; HR-TEM reveals clear lattice fringes with d-spacings indexed to spinel planes (consistent with XRD/SAED). DLS confirms a shift of the size distribution toward smaller hydrodynamic diameters and lower polydispersity relative to Co- or Fe-rich compositions. EDS maps (Co/Fe/O) demonstrate chemical

Table 8
Comparison of parameters of cobalt ferrite synthesized in the Big Solar Furnace with those of samples produced by other methods.

Parameter	Solar Furnace (This Work)	Hydrothermal [58–60]	Sol-Gel [38,61,62]	Co-precipitation [63,64]	Microemulsion [65–67]	Solid-State Sintering [22,23,68]
Method Principle	High-temperature melting using solar radiation + rapid quenching	Reaction in autoclave at T < 300°C, P > 1 atm	Formation of gel from salt solutions + heat treatment	Precipitation of metal ions with alkali + washing/calcination	Reaction in nano-reactors "water–oil–surfactant"	Mechanical mixing of oxides + high-temp fusion (>1300°C)
Phase purity $CoFe_2O_4$	Relatively high (for 1:2 stoichiometry) Advantage: Minimum secondary phases (CoO, Fe_2O_3), absence of carbon/organic impurities	Relatively high, but risk of intermediate phases (CoO, Fe_2O_3) [59]	High, but depends on calcination. Risk of carbon impurities [38]	Low–Medium Disadvantage: Incomplete precipitation, impurities, low crystallinity [63]	Relatively high, excellent stoichiometry control [66,67]	Medium–High, but secondary phases are inevitable due to incomplete reaction
Particle size	~375–480 nm (after grinding) Feature: Preservation of nanodomains after quenching	10–100 nm High crystallinity [59]	< 100 nm Good control [38]	10–50 nm (after precipitation), increases after calcination [63]	5–50 nm Highly uniform	1–10 μm Drawback: Large grains, porosity
Energy consumption	Low Advantage: Renewable solar energy use	High (autoclave)	Medium–High (calcination)	Medium (calcination)	Medium–High	Very high (long heating >1300°C)
Synthesis speed	Fast (minutes – melting + quenching)	Slow (hours/days)	Slow (days – gel aging + calcination)	Fast precipitation + slow calcination	Medium	Very slow (sintering hours + slow cooling)
Scalability	High (Industrial furnace potential)	Low (Limited by autoclave volume)	Low (Complexity in large-volume control)	High	Limited (High cost/surfactant complexity)	High (Industrial standard)
Cost	Medium Equipment (furnace) + cheap oxides	High (Expensive autoclave)	High (Expensive/toxic precursors – alkoxides)	Low (Cheap salts, alkali)	Very high (Expensive surfactants, solvents)	Low (Cheap oxides, furnace)
Structural defectiveness	Low Advantage: Clear domains, minimal defects	High (Amorphous, vacancies)	Medium	High (Amorphous, vacancies) [14]	Low	High (Pores, grain boundaries)
Specific resistivity (Ω·cm)	Very high (7.8×10^7) Advantage: Maximum at 1:2 stoichiometry [This work]	Medium (10^3–10^5)	Low–Medium (10^2–10^4)	High (10^4–10^6)	Medium (10^3–10^5)	Very high (10^6–10^8)
Eco-friendliness	Very high Key advantage: Zero CO_2 emissions, no toxic reagents/waste	Medium (Aqueous media, but energy-intensive)	Low (Toxic precursors, organic waste)	Medium (Chemical waste)	Low (Toxic surfactants, solvents, difficult disposal)	Medium–Low (High energy consumption, dust)
Key advantages	Eco-friendliness, speed, no reagent impurities, high resistivity	Morphology control, nanoscale uniformity	Homogeneity, composition control	Simplicity, low cost, scalability	Precise size/morphology control, high uniformity	Simplicity, industrial use, low raw material cost
Key disadvantages	Weather-dependent, requires large setups	Risk of intermediate phases, low speed/scalability, energy-intensive	Expensive/toxic precursors, long duration, complex organic removal	Low purity/crystallinity, stoichiometry control issues, impurities	Very high cost, cleaning difficulty, toxicity, limited scalability	Large grains, porosity, high energy cost, slow, risk of secondary phases

homogeneity in grains of No. 3 and the absence of pronounced carbon films/ligand residues after the rapid melting–quenching cycle (minute-scale heat budgets). DFT (GGA+U) calculations confirm ferrimagnetic order and a spin-polarized band gap in $CoFe_2O_4$, with pronounced p–d hybridization (O-2p with Fe/Co-3d), consistent with the increased resistivity of No. 3 and the role of defects/secondary phases in reducing ρ for non-stoichiometric compositions.

Compared with hydrothermal, sol–gel, and coprecipitation processes, the solar-thermal LSF approach provides minute-scale heat budgets, the absence of organic precursors/ligand residues (as demonstrated by HR-TEM/EDS), and a reduced risk of carbon contamination. Relative to electric furnaces, comparable or higher phase purity is achieved with lower energy consumption. At the same time, engineering challenges remain—narrowing the size distribution via closed-loop thermal control and compensating for solar-flux variability—the solution of which will improve the scalability and reproducibility of the process.

CRediT authorship contribution statement

Odiljon Abdurakhmonov: Writing – original draft, Visualization, Validation, Supervision, Software, Resources. **Kulwinder Kaur:** Writing – original draft, Visualization, Validation, Supervision, Software, Resources, Project administration, Methodology, Investigation. **Shakeel Ahmad Khandy:** Writing – original draft, Visualization, Validation, Supervision, Software, Resources, Project administration, Methodology, Investigation. **Otabek Kakhkhorov:** Visualization, Validation, Supervision, Software, Resources, Project administration. **Mirzo Sharipov:** Software, Resources, Project administration. **Muzaffar Kurbanov:** Resources, Project administration, Methodology. **Dilmurod Saidov:** Visualization, Validation, Software, Resources. **Utkirjon Sharopov:** Writing – original draft, Visualization, Validation, Supervision, Software, Resources, Project administration, Methodology, Investigation, Funding acquisition, Formal analysis, Data curation, Conceptualization. **To'raev Akbarjon:** Writing – original draft, Visualization, Validation, Resources, Methodology, Investigation, Funding acquisition, Formal analysis, Data curation. **Siddik Kakhkhorov:** Software, Resources, Project administration. **Khusniddin Juraev:** Validation, Supervision, Software, Resources, Project administration.

Declaration of Competing Interest

The authors declare that they have no known competing financial interests or personal relationships that could have appeared to influence the work reported in this paper.

Acknowledgements

We would like to express our gratitude to the Agency for Innovative Development under the Ministry of Higher Education, Science and Innovation for financial support (project No. IL-402104388). The analysis of samples by transmission electron microscopy was carried out at the Tashkent Chemical-Technological Institute in the "Scientific Laboratory of Physical and Chemical Analysis and Nanomaterials" using the HR-TEM Talos-F200i setup. We also acknowledge the use of artificial intelligence tools for ensuring high-quality scientific translation into English.

Appendix A. Supporting information

Supplementary data associated with this article can be found in the online version at doi:10.1016/j.jallcom.2025.184240.

References

[1] R. Jasrotia, J. Prakash, Y.B. Saddeek, A.H. Alluhayb, A.M. Younis, N. Lakshmaiya, C. Prakash, K.A. Aly, M. Sillanpää, Y.A.M. Ismail, A. Kandwal, P. Sharma, Cobalt ferrites: structural insights with potential applications in magnetics, dielectrics, and catalysis, Coord. Chem. Rev. 522 (2025) 216198, https://doi.org/10.1016/J.CCR.2024.216198.

[2] S.I. Ahmad, Nano cobalt ferrites: doping, structural, Low-temperature, and room temperature magnetic and dielectric properties – a comprehensive review, J. Magn. Magn. Mater. 562 (2022) 169840, https://doi.org/10.1016/J.JMMM.2022.169840.

[3] J. He, H. Yuan, M. Nie, H. Guo, H. Yu, Z. Liu, R. Sun, Soft magnetic materials for power inductors: state of art and future development, Mater. Today Electron 6 (2023) 100066, https://doi.org/10.1016/J.MTELEC.2023.100066.

[4] R. Jasrotia, K. Raj, Suman, M. Ramya, R. Kumar, D. Pathania, Y. Kumar, A. Kandwal, Magnesium ferrites and their composites based photocatalysts: synthesis approaches, effect of doping, and operational parameters on photocatalytic performance for wastewater remediation, J. Magnes. Alloy 12 (2024) 3996–4044, https://doi.org/10.1016/J.JMA.2024.10.017.

[5] E. Han, T. Gao, T. Wang, M. Bao, J. Cai, Synergy of yttrium single atom doped carbon nitride and nickel/cobalt spinel ferrites in electrochemical sensing: a novel sensor for simultaneous detection of antioxidants, J. Food Compos. Anal. 143 (2025) 107597, https://doi.org/10.1016/J.JFCA.2025.107597.

[6] O.K. Mmelesi, N. Masunga, A. Kuvarega, T.T. Nkambule, B.B. Mamba, K.K. Kefeni, Cobalt ferrite nanoparticles and nanocomposites: photocatalytic, antimicrobial activity and toxicity in water treatment, Mater. Sci. Semicond. Process 123 (2021) 105523, https://doi.org/10.1016/J.MSSP.2020.105523.

[7] O.E. Abdurakhmonov, U.B. Sharopov, S.E. Abdurakhmonov, Z.C. Kadirova, New method of chemical synthesis for nanostructured Nd-Fe-B alloy, J. Magn. Magn. Mater. 589 (2024) 171562, https://doi.org/10.1016/j.jmmm.2023.171562.

[8] O. Abdurakhmonov, U. Sharopov, S. Abdurakhmonov, Z. Kadirova, M. Karimov, M. Kurbanov, D. Saidov, Z. Iskandarov, S. Islamov, Production of High-Coercive nanostructured Nd-Fe-B alloy by chemical method, J. Magn. Magn. Mater. 600 (2024) 172130, https://doi.org/10.1016/J.JMMM.2024.172130.

[9] O.E. Abdurakhmonov, M.E. Alisultanov, S.E. Abdurakhmonov, A.G. Muradova, On the synthesis of α-Fe2O3 nanoparticles by the method of chemical deposition to obtain a magnetically hard Nd–Fe–B alloy, Nanobiotechnol. Rep. 18 (2023) 226–232, https://doi.org/10.1134/S2635167623700064.

[10] O.E. Abdurakhmonov, M.E. Alisultanov, D.A. Vertaeva, A.G. Muradova, The effect of annealing temperature on crystallization of Nd2O3 nanoparticles synthesized by the deposition method, Russ. J. Inorg. Chem. 67 (2022) 1118–1124, https://doi.org/10.1134/S0036023622070026.

[11] G. Fang, C. Liu, Y. Yang, Y. Lin, M. Xu, K. Peng, Y. Zhang, Y. Cao, Z. Liu, Y. Zhang, Enhanced microwave absorption performance of Fe3O4/Cu composites with coexistence of nanospheres and nanorods, J. Alloy. Compd. 817 (2020) 152764, https://doi.org/10.1016/J.JALLCOM.2019.152764.

[12] L. Wang, J. Li, Y. Wang, L. Zhao, Q. Jiang, Adsorption capability for Congo red on nanocrystalline MFe 2O 4 (M=Mn, Fe, Co, Ni) spinel ferrites, Chem. Eng. J. 181–182 (2012) 72–79, https://doi.org/10.1016/j.cej.2011.10.088.

[13] X. Zhao, W. Wang, Y. Zhang, S. Wu, F. Li, J.P. Liu, Synthesis and characterization of gadolinium doped cobalt ferrite nanoparticles with enhanced adsorption capability for Congo red, Chem. Eng. J. 250 (2014) 164–174, https://doi.org/10.1016/J.CEJ.2014.03.113.

[14] L. Zhuang, W. Zhang, Y. Zhao, D. Li, W. Wu, H. Shen, Temperature sensitive ferrofluid composed of mn 1-xZn xfe 2O 4 nanoparticles prepared by a modified hydrothermal process, Powder Technol. 217 (2012) 46–49, https://doi.org/10.1016/j.powtec.2011.10.007.

[15] J. Januskevicius, Z. Stankeviciute, D. Baltrunas, K. Mažeika, A. Beganskiene, A. Kareiva, Aqueous Sol-Gel synthesis of different iron ferrites: from 3D to 2D, 2021, Vol. 14, Page 1554, Mater 14 (2021) 1554, https://doi.org/10.3390/MA14061554.

[16] N.I. Abu-Elsaad, S.A. Mazen, H.M. Salem, The effect of zinc substitution and heat treatment on microstructural and magnetic properties of li ferrite nanoparticles, J. Alloy. Compd. 835 (2020) 155227, https://doi.org/10.1016/J.JALLCOM.2020.155227.

[17] G. Gong, R. Li, Y. Zhang, A. Zhang, S. Liang, S. Lu, Z. Li, Z. Wang, Wave-absorbing properties of Ni-Zn ferrites loaded on coal-based, densely porous light carbon functional materials, J. Alloy. Compd. 900 (2022) 163485, https://doi.org/10.1016/J.JALLCOM.2021.163485.

[18] C.P. Liu, M.W. Li, Z. Cui, J.R. Huang, Y.L. Tian, T. Lin, W.B. Mi, Comparative study of magnesium ferrite nanocrystallites prepared by sol-gel and coprecipitation methods, J. Mater. Sci. 42 (2007) 6133–6138, https://doi.org/10.1007/S10853-006-1070-Z/FIGURES/7.

[19] N. Das, R. Majumdar, A. Sen, H.S. Maiti, Nanosized bismuth ferrite powder prepared through sonochemical and microemulsion techniques, Mater. Lett. 61 (2007) 2100–2104, https://doi.org/10.1016/J.MATLET.2006.08.026.

[20] T. Kousar, M. Aadil, S. Zulfiqar, M.F. Warsi, S.R. Ejaz, A.Y. Elnaggar, A.M. Fallatah, S.M. El-Bahy, F. Mahmood, Wet-chemical synthesis of nanostructured Ce-doped mixed metal ferrites for the effective removal of azo dyes from industrial discharges, Ceram. Int. 48 (2022) 11858–11868, https://doi.org/10.1016/J.CERAMINT.2022.01.057.

[21] A. Scano, V. Cabras, M. Pilloni, G. Ennas, Microemulsions: the renaissance of ferrite nanoparticle synthesis, J. Nanosci. Nanotechnol. 19 (2019) 4824–4838, https://doi.org/10.1166/JNN.2019.16876.

[22] M. Rahmani, O. Mirzaee, M. Tajally, M.R. Loghman-Estarki, A comparative study of synthesis and spark plasma sintering of YAG nano powders by different co-

precipitation methods, Ceram. Int. 44 (2018) 10035–10046, https://doi.org/10.1016/J.CERAMINT.2018.02.148.
[23] O. Guillon, J. Gonzalez-Julian, B. Dargatz, T. Kessel, G. Schierning, J. Räthel, M. Herrmann, Field-assisted sintering technology/spark plasma sintering: mechanisms, materials, and technology developments, Adv. Eng. Mater. 16 (2014) 830–849, https://doi.org/10.1002/ADEM.201300409;JOURNAL:JOURNAL:15272648;WGROUP:STRING:PUBLICATION.
[24] C. Liu, Y. Zhang, H. Gong, Y. Hu, S. Duan, K. Peng, K. Zhu, Facile fabrication of rGO/Zr4+-Ni2+ gradient-doped BaM composites for broad microwave absorption bandwidth, Ceram. Int. 47 (2021) 4333–4337, https://doi.org/10.1016/J.CERAMINT.2020.09.273.
[25] J. Gao, Z. Ma, F. Liu, X. Weng, K. Meng, Preparation and microwave absorption properties of Gd–Co ferrite@silica@carbon multilayer core–shell structure composites, Chem. Eng. J. 446 (2022) 137157, https://doi.org/10.1016/J.CEJ.2022.137157.
[26] B. Chen, M. Zhou, T. Jiang, L. Li, Observation of diffusion behavior between Cr2O3 and calcium ferrite based on diffusion couple method at 1373 K, J. Alloy. Compd. 802 (2019) 103–111, https://doi.org/10.1016/J.JALLCOM.2019.06.137.
[27] H.L. Andersen, C. Granados-Miralles, K.M.Ø. Jensen, M. Saura-Múzquiz, M. Christensen, The chemistry of spinel ferrite nanoparticle nucleation, crystallization, and growth, ACS Nano 18 (2024) 9852–9870, https://doi.org/10.1021/acsnano.3c08772.
[28] M. Zain Ul Abidin, M. Ikram, S. Moeen, G. Nazir, M.B. Kanoun, S. Goumri-Said, A comprehensive review on the synthesis of ferrite nanomaterials via bottom-up and top-down approaches advantages, disadvantages, characterizations and computational insights, Coord. Chem. Rev. 520 (2024) 216158, https://doi.org/10.1016/j.ccr.2024.216158.
[29] Q.Y. Tamboli, P.D. Mhase, I. Bushnak, A.M. Alshehri, A.G. Al-Sehemi, S. M. Patange, K.R. Zakde, Eco-friendly sol-gel synthesis and comprehensive analysis of Ruthenium-substituted cobalt ferrite nanoparticles using moringa oleifera gum, Solid State Sci. 168 (2025) 108041, https://doi.org/10.1016/j.solidstatesciences.2025.108041.
[30] V.C. Pujari, P.D. Mhase, S.D. Balgude, S.S. Jadhav, S.J. Gilani, P.S. More, S. E. Shirsath, S.F. Shaikh, S.M. Patange, Eco-friendly synthesis, comprehensive characterization and photocatalytic efficiency of rare earth-substituted M-type hexaferrites for visible-light-driven dye degradation, Ceram. Int. 51 (2025) 39866–39885, https://doi.org/10.1016/j.ceramint.2025.06.221.
[31] P.D. Mhase, V.C. Pujari, S.E. Shirsath, A.V. Fulari, S.S. Jadhav, C.V. Ramana, S. M. Patange, Advances in M-type hexaferrites: a review tailoring structural, magnetic, and microwave absorption properties for emerging technologies, Coord. Chem. Rev. 541 (2025) 216825, https://doi.org/10.1016/j.ccr.2025.216825.
[32] V.C. Pujari, P.D. Mhase, R.M. Mahindrakar, S.S. Meena, S.R. Kamble, S.M. Patange, S.S. Jadhav, Modifications in structure dependent magnetic parameters of Nd-doped Ba–Ca hexaferrites synthesized by sol gel using lemon extract as a fuel, Ceram. Int. 49 (2023) 40466–40477, https://doi.org/10.1016/j.ceramint.2023.10.023.
[33] V.C. Pujari, P.D. Mhase, S. Balgude, P. More, S.S. Jadhav, S.M. Patange, Energy band gap tuning of Ba-Ca hexagonal ferrite by Dy3+ ion substitution ($0 \leq x \leq 0.2$) to improve spectral, structural, dielectric and photocatalytic properties, Ceram. Int. 50 (2024) 53351–53361, https://doi.org/10.1016/j.ceramint.2024.10.186.
[34] V.C. Pujari, P.D. Mhase, S.S. Meena, S.S. Jadhav, S.E. Shirsath, A.M. Al-Enizi, S. M. Patange, Tailoring structural and magnetic properties of Ba0.5Sr0.5RuXFe12-xO19 hexaferrites with Ru3+ substitution, Ceram. Int. 51 (2025) 22129–22141, https://doi.org/10.1016/j.ceramint.2025.02.375.
[35] J. Wu, D. Zhang, X. Xu, Y. Shen, J. Yuan, Y. Zhang, L. Hu, Preparation, microstructure and properties of ceramic slab tiles by solar furnace, Constr. Build. Mater. 475 (2025) 141155, https://doi.org/10.1016/j.conbuildmat.2025.141155.
[36] D. Guo, H. Liu, C. Zang, Y. Wang, F. Sun, D. Lei, J. Wu, H. Zhu, Z. Wang, Experimental study on the direct firing of ceramic ware using concentrated solar energy, IScience 27 (2024) 110222, https://doi.org/10.1016/j.isci.2024.110222.
[37] Y. A Abdel Hadi, Y. Sobirov, S. Makhmudov, Using the big solar furnace as an astronomical telescope, Phys. Astron. Int. J. 5 (2021) 28–35, https://doi.org/10.15406/paij.2021.05.00231.
[38] N.B. Gatchakayala, R.S.R. Dachuru, Synthesis of CoFe2O4 nanomaterials via Sol–Gel Auto-Combustion method using different chelating agent, and its effects on magnetic and dielectric properties, Phys. Status Solidi 260 (2023) 2300010, https://doi.org/10.1002/PSSB.202300010.
[39] U. Sharopov, K. Samiev, M. Kurbanov, M. Karimov, D. Saidov, F. Akbarova, Z. Iskandarov, S. Islamov, A. Komolov, S. Pshenichnyuk, Tuning surface charge and defects in zinc oxide crystals via Low-Energy electron irradiation, J. Surf. Invest. 18 (2024) S311–S320, https://doi.org/10.1134/S1027451024702227/FIGURES/11.
[40] A.A. Abdurakhmanov, M.S. Paizullakhanov, Z. Akhadov, Synthesis of calcium aluminates on the big solar furnace, Appl. Sol. Energy (Engl. Transl. Gelio) 48 (2012) 129–131, https://doi.org/10.3103/S0003701X12020041/METRICS.
[41] A.A. Abdurakhmanov, S.A. Faiziev, R.Y. Akbarov, S.K. Suleimanov, M.K. Rumi, M. S. Paizullakhanov, E.Z. Nodirmatov, Properties of pyroxene glass ceramics, heat treated in the big solar furnace, Appl. Sol. Energy (Engl. Transl. Gelio) 45 (2009) 45–47, https://doi.org/10.3103/S0003701X09010125/METRICS.
[42] M.S. Payzullakhanov, S.D. Payziyev, S.K. Suleymanov, Modeling of processes of heating and cooling of materials in a solar furnace, Appl. Sol. Energy (Engl. Transl. Gelio) 55 (2019) 404–408, https://doi.org/10.3103/S0003701X19060082/FIGURES/6.
[43] Solar Furnace in Parkent (near Tashkent), (n.d.). ⟨https://www.orexca.com/uzbekistan/tashkent/sun_institute_parkent.htm⟩ (accessed September 8, 2025).
[44] I. Sharifi, H. Shokrollahi, M.M. Doroodmand, R. Safi, Magnetic and structural studies on CoFe2O4 nanoparticles synthesized by co-precipitation, normal micelles and reverse micelles methods, J. Magn. Magn. Mater. 324 (2012) 1854–1861, https://doi.org/10.1016/J.JMMM.2012.01.015.
[45] J. Singh, K. Kaur, M.A. Bhat, U.B. Sharopov, S. Dhiman, M. Goyal, S.S. Verma, S. A. Khandy, First-principles calculations on the electronic structure and thermoelectric properties of quaternary heusler compounds: LiScPtSi and LiScPdGe, Mater. Today Commun. 32 (2022) 103961, https://doi.org/10.1016/J.MTCOMM.2022.103961.
[46] S.A. Khandy, I. Islam, K. Kaur, A.M. Ali, A.F.A. El-Rehim, Electronic structure, stability, photocatalytic and optical properties of new lead-free double perovskites Tl2PtX6 (X = Cl, Br) for light-harvesting applications, Mater. Chem. Phys. 297 (2023) 127293, https://doi.org/10.1016/j.matchemphys.2023.127293.
[47] J. Singh, K. Kaur, S.A. Khandy, S. Dhiman, M. Goyal, S.S. Verma, Structural, electronic, mechanical, and thermoelectric properties of <scp>LiTiCoX</scp> (X = Si, Ge) compounds, Int. J. Energy Res 45 (2021) 16891–16900, https://doi.org/10.1002/er.6851.
[48] A.F. Wani, B. Rani, S. Dhiman, U.B. Sharopov, K. Kaur, SiH monolayer: a promising two-dimensional thermoelectric material, Int. J. Energy Res. 46 (2022) 10885–10893, https://doi.org/10.1002/er.7889.
[49] O. Abdurakhmonov, M. Aripova, F. Erkinov, S. Abdurakhmonov, U. Sharopov, M. Karimov, M. Kurbanov, D. Saidov, Z. Pędzich, D. Kozien, T.A. Kurniawan, E. Bondar, Green synthesis of high-purity hexagonal boron nitride nanoparticles, Vacuum 239 (2025) 114386, https://doi.org/10.1016/J.VACUUM.2025.114386.
[50] U. Sharopov, K. Samiev, A. To'raev, M. Kurbanov, M. Karimov, D. Saidov, F. Akbarova, S. Turopova, Z. Iskandarov, S. Islamov, A. Komolov, I. Pronin, H. Bandarenka, O. Abdurakhmonov, S. Abdurakhmonov, M. Srinivasan, K. Kaur, Exploring electron energy dependencies in the formation of surface charge on ZnO crystals, Vacuum 227 (2024) 113395, https://doi.org/10.1016/J.VACUUM.2024.113395.
[51] A. Omelyanchik, M. Salvador, F. D'orazio, V. Mameli, C. Cannas, D. Fiorani, A. Musinu, M. Rivas, V. Rodionova, G. Varvaro, D. Peddis, Magnetocrystalline and surface anisotropy in cofe2o4 nanoparticles, Nanomaterials 10 (2020) 1–11, https://doi.org/10.3390/nano10071288.
[52] D. Peddis, M.V. Mansilla, S. Mørup, C. Cannas, A. Musinu, G. Piccaluga, F. D'Orazio, F. Lucari, D. Fiorani, Spin-canting and magnetic anisotropy in ultrasmall CoFe2O 4 nanoparticles, J. Phys. Chem. B 112 (2008) 8507–8513, https://doi.org/10.1021/jp8016634.
[53] B.B. Patil, A.D. Pawar, D.B. Bhosale, J.S. Ghodake, J.B. Thorat, T.J. Shinde, Effect of La3+ substitution on structural and magnetic parameters of Ni–Cu–Zn nano-ferrites, J. Nanostructure Chem. 9 (2019) 119–128, https://doi.org/10.1007/s40097-019-0302-0.
[54] S. Rasheed, R.A. Khan, F. Shah, B. Ismail, J. Nisar, S.M. Shah, A. Rahim, A.R. Khan, Enhancement of electrical and magnetic properties of cobalt ferrite nanoparticles by co-substitution of Li-Cd ions, J. Magn. Magn. Mater. 471 (2019) 236–241, https://doi.org/10.1016/j.jmmm.2018.09.073.
[55] T. Lakshmigandhan, S. Nithiyanantham, S. Mahalakshmi, K. Kogulakrishnan, R. Mohan, B. Gunasekaran, L. Palaniappan, Structural, electrical and magnetic studies on CoFe2O4 nanoparticles with polyvinylalcohol (PVA) via Sol-Gel approach, Mater. Sci. Eng. B 307 (2024) 117494, https://doi.org/10.1016/j.mseb.2024.117494.
[56] A.B. Rajput, S. Hazra, N.N. Ghosh, Synthesis and characterisation of pure single-phase CoFe2O4 nanopowder via a simple aqueous solution-based EDTA-precursor route, J. Exp. Nanosci. 8 (2013) 629–639, https://doi.org/10.1080/17458080.2011.582170.
[57] R. Dhyani, R.C. Srivastava, G. Dixit, Study of magnetic and Temperature-Dependent dielectric properties of Co-CuFe2O4 nanoferrites, J. Electron. Mater. 51 (2022) 5492–5507, https://doi.org/10.1007/s11664-022-09831-0.
[58] Z. Rahimi, H. Sarafraz, G. Alahyarizadeh, A.S. Shirani, Hydrothermal synthesis of magnetic CoFe2O4 nanoparticles and CoFe2O4/MWCNTs nanocomposites for u and pb removal from aqueous solutions, J. Radioanal. Nucl. Chem. 317 (2018) 431–442, https://doi.org/10.1007/S10967-018-5894-1/TABLES/4.
[59] D. Zhao, X. Wu, H. Guan, E. Han, Study on supercritical hydrothermal synthesis of CoFe2O4 nanoparticles, J. Supercrit. Fluids 42 (2007) 226–233, https://doi.org/10.1016/J.SUPFLU.2007.03.004.
[60] N.M. Refat, M.Y. Nassar, S.A. Sadeek, A controllable one-pot hydrothermal synthesis of spherical cobalt ferrite nanoparticles: synthesis, characterization, and optical properties, RSC Adv. 12 (2022) 25081–25095, https://doi.org/10.1039/D2RA03345C.
[61] J. Venturini, R.Y.S. Zampiva, S. Arcaro, C.P. Bergmann, Sol-gel synthesis of substoichiometric cobalt ferrite (CoFe2O4) spinels: influence of additives on their stoichiometry and magnetic properties, Ceram. Int. 44 (2018) 12381–12388, https://doi.org/10.1016/J.CERAMINT.2018.04.026.
[62] T. Saragi, S. Nurjannah, R. Novia, N. Syakir, E. Simanjuntak, L. Safriani, Risdiana, A. Bahtiar, Synthesis of cobalt ferrite particles by utilized sol-gel method, Mater. Sci. Forum 827 (2015) 219–222, https://doi.org/10.4028/WWW.SCIENTIFIC.NET/MSF.827.219.
[63] P. Roy, S.M. Hoque, S. Akter, S.I. Liba, S. Choudhury, Study on the chemical co-precipitation synthesized CoFe2O4 nanoparticle for magnetocaloric performance in the vicinity of superparamagnetic blocking temperature, Heliyon 10 (2024) e34413, https://doi.org/10.1016/J.HELIYON.2024.E34413.
[64] M.S. S, K.S. B, T.S. M, K.A. E, Synthesis, Structural and Magnetic Properties of Cobalt Ferrite (CoFe2O4) Nanoparticles by Simple Co-precipitation Technique, (n. d.). https://doi.org/10.5281/ZENODO.7763129.
[65] P. Laokul, S. Arthan, S. Maensiri, E. Swatsitang, Magnetic and optical properties of CoFe2O4 nanoparticles synthesized by reverse micelle microemulsion method, J. Supercond. Nov. Magn. 28 (2015) 2483–2489, https://doi.org/10.1007/S10948-015-3068-8/FIGURES/7.

[66] V. Pillai, D.O. Shah, Synthesis of high-coercivity cobalt ferrite particles using water-in-oil microemulsions, J. Magn. Magn. Mater. 163 (1996) 243–248, https://doi.org/10.1016/S0304-8853(96)00280-6.
[67] F. Foroughi, S.A. Hassanzadeh-Tabrizi, J. Amighian, Microemulsion synthesis and magnetic properties of hydroxyapatite-encapsulated nano CoFe2O4, J. Magn. Magn. Mater. 382 (2015) 182–187, https://doi.org/10.1016/J.JMMM.2015.01.075.
[68] N. Millot, S. Le Gallet, D. Aymes, F. Bernard, Y. Grin, Spark plasma sintering of cobalt ferrite nanopowders prepared by coprecipitation and hydrothermal synthesis, J. Eur. Ceram. Soc. 27 (2007) 921–926, https://doi.org/10.1016/J.JEURCERAMSOC.2006.04.141.
[69] D. Cao, L. Pan, J. Li, X. Cheng, Z. Zhao, J. Xu, Q. Li, X. Wang, S. Li, J. Wang, Q. Liu, Investigation on the structures and magnetic properties of carbon or nitrogen doped cobalt ferrite nanoparticles, Sci. Rep. 8 (2018) 1–9, https://doi.org/10.1038/s41598-018-26341-4.
[70] K. Dhabekar, K.M. Kant, Structural and dielectric properties of cobalt ferrite based nanocomposites, Phys. B Condens. Matter 603 (2021) 412752, https://doi.org/10.1016/j.physb.2020.412752.
[71] T. Dippong, E.A. Levei, O. Cadar, Recent advances in synthesis and applications of MFe2O4 (M = Co, Cu, Mn, Ni, Zn) nanoparticles, Nanomaterials 11 (2021) 1560, https://doi.org/10.3390/nano11061560.
[72] S.M. Ansari, K.C. Ghosh, R.S. Devan, D. Sen, P.U. Sastry, Y.D. Kolekar, C. V. Ramana, Eco-Friendly synthesis, crystal chemistry, and magnetic properties of Manganese-Substituted CoFe2O4Nanoparticles, ACS Omega 5 (2020) 19315–19330, https://doi.org/10.1021/acsomega.9b02492.